DIPLOMARBEIT

Titel der Diplomarbeit

Three-Dimensional Modeling of a Nanowire Field-Effect Biosensor (BioFET)

angestrebter akademischer Grad

Magister der Naturwissenschaften (Mag. rer. nat.)

Verfasser:	Stefan Andreas Baumgartner
Matrikel-Nummer:	A 0502280
Studienrichtung:	Mathematik
Betreuer:	Dr. Clemens Heitzinger

Wien, Juni 2009

Acknowledgements

First of all I want to thank all the people who supported me in my studies, with my diploma thesis or in my life and also those who are not mentioned by name in the following.

First I thank my adviser Clemens Heitzinger for giving me the chance to write my diploma thesis with the support of his FWF (Austrian Science Fund) project and that he always had time for me to give me advice. I also thank many other WPI (Wolfgang Pauli Institute) members for taking me in very well and in particular WPI director Norbert Mauser, who helped me with my requests and my mathematical problems, and Alena Bulyha, who worked with me in this project and with whom I discussed many ideas.

Furthermore I thank my family for giving me the required background and primarily my parents Gertrude and Anton Baumgartner who made my studies possible at all.

Finally I thank all my friends for supporting me in my daily life.

Abstract

This work deals with the modeling and simulation of a biologically sensitive field-effect transistor, a so called BioFET.

Since the functioning of BioFETs is not completely understood, there is a great interest in mathematical and physical models which lead to a quantitative understanding. In this work, a mathematical model for a nanowire field-effect biosensor is developed to gain insight into its physical behavior.

In the following we will describe the model equations as well as their discretization. The basic equation of our model is the Poisson equation for the electrostatic interaction of the charge carriers. Furthermore we use the drift-diffusion equations for the dynamics in the semiconductor and a Boltzmann model for the liquid. The interface conditions are resolved with a homogenization method where the continuity conditions at the interface are replaced with jump conditions. The discretization methods used for this work are the finite-volume method and the Scharfetter-Gummel method for the drift-diffusion equations. Finally the numerical algorithm and simulation results are shown in detail.

This work is organized as follows:

- **Chapter 1** gives an introduction to biosensors and their functionality. Also the advantages of biosensors and the mathematical problems in their modeling are described.

- **Chapter 2** defines the model used in our simulations, based on the Poisson equation coupled to the drift-diffusion equations. We also use the Poisson-Boltzmann term to include screening in ionic solutions. At the end the variables and their units are summarized.

- **Chapter 3** explains the discretization methods: the finite-volume method and the Scharfetter-Gummel algorithm.

- **Chapter 4** describes the discretization of the model equations. Interface conditions are obtained from homogenization.

- **Chapter 5** illustrates the modifications of the discretization, which are on the one hand necessary to get a linear equation system for the potential

and on the other hand necessary for a fast implementation.

- **Chapter 6** specifies the numerical algorithm used for the simulations in pseudo-code.

- **Chapter 7** varies different simulation parameters and shows the numerical results for the electric potential, the hole and the electron density, the current flow, and the source-drain current.

Zusammenfassung

Diese Arbeit behandelt einen biologisch sensitiven Feldeffekttransistor, einen sogenannten BioFET.

Weil die Funktionalität solcher BioFETs noch nicht vollständig verstanden wurde herrscht ein großes Interesse an mathematischen und physikalischen Modellen, welche zu einem quantitativen Verständnis führen. In dieser Arbeit wurde ein mathematisches Modell erarbeitet um mehr Einsicht in das physikalische Verhalten zu bekommen.

Im Folgenden werden wir die Modellgleichungen und die Diskretisierung beschreiben. Die Gleichung von der wir ausgehen, ist die Poisson Gleichung. Weiters benutzen wir die Drift-Diffusions Gleichungen als Halbleitergleichungen und ein Boltzmann Modell für die wässrige Lösung. Die Stetigkeitsbedingungen an der Schnittstelle werden mittels einer Homogenisierungsmethode durch Sprungbedingungen ersetzt. Die für die Diskretisierung benutzten Methoden sind die finite Volumen Methode und die Scharfetter-Gummel Methode für die Drift-Diffusionsgleichungen. Als Abschluss werden der numerische Algorithmus sowie die numerischen Resultate präsentiert.

Diese Arbeit ist auf folgende Weise strukturiert:

- **Kapitel 1** gibt eine Einführung in das Thema Biosensoren und deren Funktionsweise. Weiters werden die Vorteile von Biosensoren und die mathematischen Probleme, die sie verusachen, beschrieben.

- **Kapitel 2** definiert das, für unsere Simulationen verwendete, Modell. Hierbei verwenden wir als Grundlage die Poisson Gleichung und für den Halbleiterteil die Drift-Diffusions-Gleichungen. Wir verwenden auch den Poisson-Boltzmann Term um eine Rasterung in ionischen Lösungen zu erhalten. Im Anhang werden die Variablen und ihre Einheiten zusammengefasst.

- **Kapitel 3** zeigt die verwendeten Methoden zur Diskretisierung. Diese sind die finite Volumen und die Scharfetter-Gummel Methode.

- **Kapitel 4** beschreibt die Diskretisierung der Modellgleichungen. Die Schnittstellenbedingungen werden durch eine Homogenisierungsmethode

bestimmt.

- **Kapitel 5** erläutert die benutzten Modifikationen der Diskretisierung, welche einerseites notwendig waren, um ein lineares System für die Gleichungen des Potentials zu bekommen und andererseits notwendig um die Geschwindigkeit des Programms zu erhöhen.

- **Kapitel 6** beschreibt den, für die Simulationen benutzten, Programmalgorithmus.

- **Kapitel 7** benutzt verschiedene Werte für Simulationen und zeigt die daraus folgenden numerischen Resultate für das elektrische Potential, die Löcher- und Elektronendichte, dem Stromfluss und dem Strom zwischen den Kontakten.

Contents

1 Introduction

Since the first biosensor was developed by Clark in 1962, many efforts have been made to create functional hybrid systems [9]. Hence many different types of biosensors have been created. One of the most attractive approaches is the use of an ISFET (ion-selective field-effect transistor). Bergveld invented the ISFET in 1970 and up to this day the interest in ISFET-based biosensors, so called biologically modified field-effect transistors (BioFETs), is enormous. The range of applications reaches from biomedicine, biotechnology, food and drug industry, environmental monitoring and process technology to defense and security [10].

These BioFETs belong to the class of electrochemical biosensors, which are sensors with an electrochemical transducer. A more precise definition of a BioFET is given by the International Union of Pure and Applied Chemistry (IUPAC): An electrochemical biosensor is a self-contained integrated device, which is capable of providing specific quantitative or semi-quantitative analytical information using a biological recognition element (biochemical receptor) which is retained in direct spatial contact with an electrochemical transduction element [13]. The idea behind such biosensors is to transform biochemical information into a physical or chemical signal. Therefore the electronic conducting, semiconducting or ionic conducting material is coated with a biochemical film. Some examples for such biological recognition elements are enzymes, biological ionophores, antibodies, plant or animal tissues, whole cells and proteins.
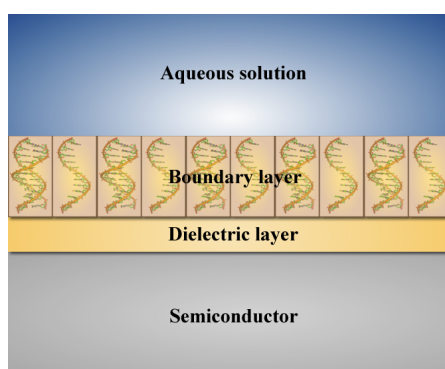

Figure 1.1: Schematic diagram of a nanowire BioFET [2].

Figure 1.1 shows how a BioFET works. The transducer is a semiconductor layer which is surrounded by a dielectric layer. In our model it consists of silicon and is surrounded by silicon oxide. Furthermore there is a biofunctionalized surface which we call the boundary layer. For example, a DNA sensor uses ssDNA (single-stranded deoxyribonucleic acid) as recognition elements and the complementary strands as target molecules. After hybridization of the DNA strands, the charge distribution in the boundary layer changes and can be measured through the conductance of the semiconductor.

The main advantage of BioFETs is label-free operation, i.e., no fluorescent or radioactive markers are needed. Further advantages are high sensitivity, real-time operation and high selectivity [15].

Several facts have to be taken into account for the modeling and simulation of BioFETs. First we have to connect two systems: the biological system, i.e., the biofunctionalized surface layer, and an electronic system, i.e., the semiconductor transducer. Another fact is that we have a multiscale problem. On the one hand, the recognition elements on the functionalized surface are only up to a few nanometers large. On the other hand, the length of the biosensor can be a few micrometers. The problem with these multiple length scales is that they require an extremely fine grid. To solve this problem, we homogenize the boundary layer between the oxide and the liquid solution [2].

Our biosensor model is based on experimental structures [4, 11, 12]. Figure 1.2 shows such a structure including the source contact, the drain contact, the backgate at the bottom, and the nanowire.
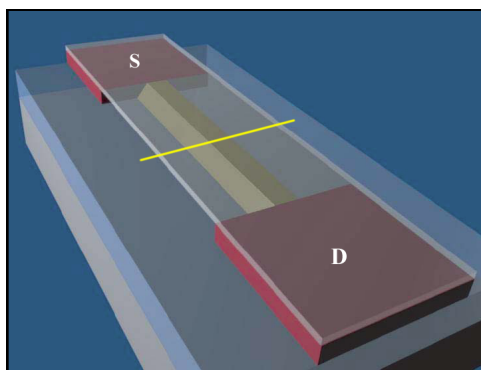

Figure 1.2: An experimental BioFET structure [11].

2 The model

In this chapter we describe the model equations related to Figure 1.2.

2.1 The three-dimensional model of the nanowire biosensor

Figure 2.1 shows the cross section through the biosensor which is marked in Figure 1.2 by a yellow line. To simplify the following descriptions, we define the
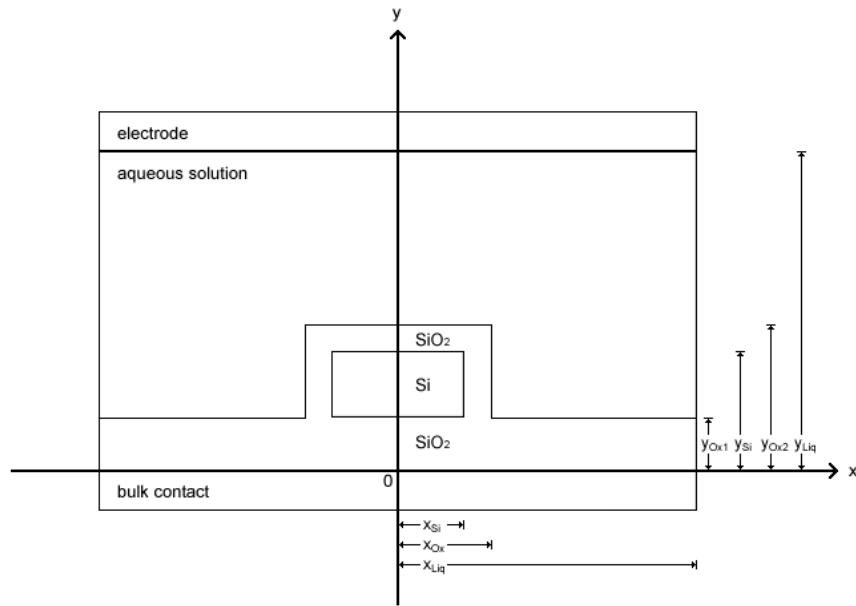

Figure 2.1: A cross section through the nanowire biosensor.

following domains:

- The silicon-oxide domain:
  $\Omega_{Ox} := [-x_{Liq}, x_{Liq}] \times (0, y_{Ox1}) \times [O, L_z] \cup (-x_{Ox}, -x_{Si}) \times [y_{Ox1}, y_{Si}] \times [0, L_z]$
  $\cup (x_{Si}, x_{Ox}) \times [y_{Ox1}, y_{Si}] \times [0, L_z] \cup (-x_{Ox}, x_{Ox}) \times (y_{Si}, y_{Ox2}) \times [0, L_z]$.

- The silicon domain:
  $\Omega_{Si} := [-x_{Ox}, x_{Ox}] \times [y_{Ox1}, y_{Si}] \times [0, L_z]$.

- The liquid domain:
  $\Omega_{Liq} := [-x_{Liq}, x_{Liq}] \times [y_{Ox2}, y_{Liq}] \times [0, L_z] \cup [-x_{Liq}, -x_{Ox}] \times [y_{Ox1}, y_{Ox2}] \times [0, L_z]$
  $\cup [x_{Ox}, x_{Liq}] \times [y_{Ox1}, y_{Ox2}] \times [0, L_z]$.

- The whole biosensor $\Omega := \Omega_{Ox} \cup \Omega_{Si} \cup \Omega_{Liq}$.

- The interface between the liquid area and the oxide area $\Delta := \partial\Omega_{Ox} \cap \partial\Omega_{Liq}$.

2.2 The model equations

In this section we give equations for the electric potential V, the concentration n of the electrons, and the concentration p of the holes. All other values are constants which are shown in Table 2.1 at the end of this section.

The main equation for the electric potential V is the mean-field Poisson equation

$$-\nabla \cdot (\varepsilon(x)\nabla V(x)) = \tilde{n}(x) \tag{2.1}$$

where $x \in \mathbb{R}^3$, ε is the permittivity, and $\tilde{n}$ is the charge distribution.

The permittivity ε is defined as the piecewise constant function

$$\varepsilon(x) := \begin{cases} \varepsilon_{Ox} \in \mathbb{R} & \text{for } x \in \Omega_{Ox}, \\ \varepsilon_{Si} \in \mathbb{R} & \text{for } x \in \Omega_{Si}, \\ \varepsilon_{Liq} \in \mathbb{R} & \text{for } x \in \Omega_{Liq}. \end{cases} \tag{2.2}$$

For the charge distribution $\tilde{n}$ we have three different models: the doping of the semiconductor and the electrons and the holes in the domain Ω_{Si}, the ions in the liquid in the domain Ω_{Liq}, and the equation for the dielectric layer in the domain Ω_{Ox}. Hence we have the partition

$$\tilde{n}(x) := \begin{cases} n_{Ox}(x) & \text{for } x \in \Omega_{Ox}, \\ n_{Si}(x) & \text{for } x \in \Omega_{Si}, \\ n_{Liq}(x) & \text{for } x \in \Omega_{Liq}. \end{cases} \tag{2.3}$$

For the silicon domain we use the drift-diffusion model [5], which is the set of

equations

$$
\begin{aligned}
n_{Si}(x) &= C(x) + p(x) - n(x), \\
\nabla \cdot J_n &= R, \\
\nabla \cdot J_p &= -R, \\
J_n &= D_n \nabla n - \mu_n n \nabla V, \\
J_p &= -D_p \nabla p - \mu_p p \nabla V,
\end{aligned}
\tag{2.4}
$$

where C is the doping concentration, n and p are the concentrations of the free carriers, namely electrons and holes, J_n and J_p are the densities of the electron and hole currents, D_n and D_p are the diffusion coefficients, and μ_n and μ_p are the mobilities of electrons and holes. The second and the third equation are for the charge sources given by the recombination rate R, which is in our model the Shockley-Read-Hall term

$$
R = \frac{np - n_i^2}{\tau_p(n + n_i) + \tau_n(p + n_i)},
\tag{2.5}
$$

where τ_n and τ_p are the lifetimes of electrons and holes and n_i is the intrinsic charge density of the semiconductor material. Furthermore we use the Einstein relations

$$
\begin{aligned}
D_n &= U_T \mu_n, \\
D_p &= U_T \mu_p,
\end{aligned}
\tag{2.6}
$$

for the diffusion coefficients where U_T is the thermal voltage and has a value of $\approx 0.025V$ for silicon at room temperature.

In the oxide we set only $n_{Ox}(x) := 0$ and in the liquid we have

$$
n_{Liq}(x) := \sum_{\sigma \in \{-1,1\}} \alpha \sigma f_\sigma e^{-\sigma \beta V(x)},
\tag{2.7}
$$

which is a Boltzmann model. This Boltzmann model describes the screening in ionic solutions. Here f_σ stands for the exponential of the chemical potentials Φ_σ, i.e., $f_\sigma = e^{\sigma \beta \Phi_\sigma}$ and $\beta := q/(kT)$, where q is the elementary charge, k is the Boltzmann constant, and T is the temperature. Furthermore α is the Na^+Cl^- concentration in the liquid.

At the interface Δ we replace the continuity condition for the potential and the continuity condition for the electric displacement using a homogenization method

[2] by the following jump conditions

$$V(x+) - V(x-) = \frac{D}{\varepsilon(x+)}, \tag{2.8}$$

$$\varepsilon_{Liq}\nabla V(x+) - \varepsilon_{Ox}\nabla V(x-) = -C_s \tag{2.9}$$

where $x+$ denotes the limes from the liquid to the interface and $x-$ denotes the limes from the silicon oxide to the interface (see Figure 2.2).
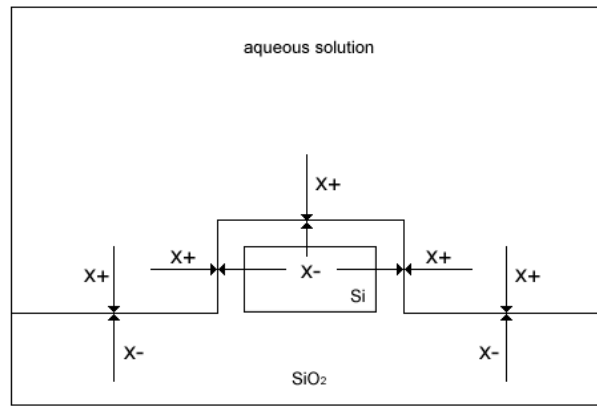

Figure 2.2: Vectors pointing to the interface.

Here D is the macroscopic dipole moment density and C_s is the macroscopic surface charge density which are shown in [2]. Here we treat them as given constants.

The boundary $\partial\Omega$ of the biosensor has Dirichlet conditions at the backgate, at the electrode, and at the source and drain contacts, and Neumann boundary conditions everywhere else. The source and the drain contacts are Ohmic contacts, hence the space charge vanishes, i.e., $C + p - n = 0$, and the system is in thermal equilibrium, i.e., $np = n_i^2$. The quasi Fermi levels Φ_n and Φ_p are defined by

$$\Phi_n := V - U_T \ln\left(\frac{n}{n_i}\right),$$

$$\Phi_p := V + U_T \ln\left(\frac{p}{n_i}\right) \tag{2.10}$$

and the values of the applied voltage U at Ohmic contacts are assumed as $\Phi_n = U = \Phi_p$. Hence we get the boundary conditions

$$
\begin{aligned}
n(x) &= \frac{1}{2}(C + \sqrt{C^2 + 4n_i^2}), \\
p(x) &= \frac{1}{2}(-C + \sqrt{C^2 + 4n_i^2}), \\
V(x) &= U + U_T \log\left(\frac{n(x)}{n_i}\right) = U - U_T \ln\left(\frac{p(x)}{n_i}\right)
\end{aligned}
\tag{2.11}
$$

at the Ohmic contacts.
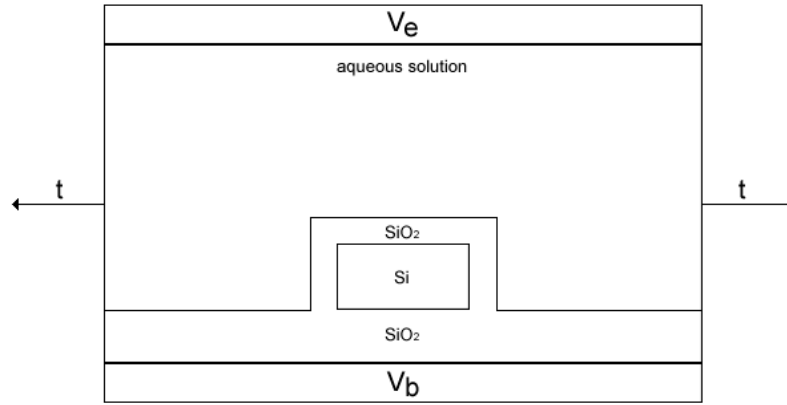
Figure 2.3: Boundary conditions at the electrode and at the backgate and the outward pointing normal vector t.

The Neumann conditions

$$
\nabla V(x) \cdot t = 0
\tag{2.12}
$$

are used everywhere else, where t is the outward pointing normal vector. At last we have the Dirichlet conditions

$$
\begin{aligned}
V(x) &= V_b, \\
V(x) &= V_e
\end{aligned}
\tag{2.13}
$$

at the boundaries of the backgate and the electrode.

2.3 Variables and units

The following table shows the variables and their units used in this model.

Meaning	Variable	Unit or value
Temperature	T	K
Elementary charge	q	$q = 1.60218 \cdot 10^{-19}$C
Boltzmann constant	k	$8.31452 \cdot 10^{-3}$kJ $\cdot$ mol^{-1} $\cdot$ K^{-1}
Electric potential	V, U, Φ	kJ $\cdot$ mol^{-1} $\cdot$ q^{-1} = 0.010364272V
Charge density	n, p	$q \cdot$ nm^{-3}
Macroscopic surface charge density	C_s	$q \cdot$ nm^{-2}
Macroscopic dipole moment density	D	$q \cdot$ nm^{-1}
Electron lifetime	τ_n	10^6ps (silicon)
Hole lifetime	τ_p	10^7ps (silicon)
Electron low-field mobility	μ_n	$1.5 \cdot 10^5$nm^2 $\cdot$ V^{-1} $\cdot$ ps^{-1} (silicon)
Hole low-field mobility	μ_p	$4.5 \cdot 10^4$nm^2 $\cdot$ V^{-1} $\cdot$ ps^{-1} (silicon)
Diffusion coefficient	D_n, D_p	nm^2 $\cdot$ ps^{-1}
Current flow	J	$q \cdot$ nm^2 $\cdot$ ps^{-1}
Recombination rate	R	$q \cdot$ nm^2 $\cdot$ ps^{-1}
Permittivity of silicon	ε_{Si}	$11.9\varepsilon_0$
Permittivity of silicon oxide	ε_{Ox}	$3.9\varepsilon_0$
Permittivity of water	ε_{Liq}	$80.1\varepsilon_0$
Thermal voltage	U_T	0.025V
Doping concentration	C	$q \cdot$ nm^{-3}

Table 2.1: The variables and their units.

3 Discretization methods

3.1 The finite-volume method

In this section we follow the explanations of [3]. The finite-volume method is a discretization method that is especially advantageous for numerical investigations of partial differential equations in divergence form

$$\partial_t S(u) + \nabla \cdot (M(u) - K(\nabla u)) = Q(u), \tag{3.1}$$

where S is a storage term, M is a convective part, K is a diffusive part, and Q is a source term. S, M, K, and Q can depend linearly or nonlinearly on u. It is also useful for partial differential equations where parts are in divergence form, for instance parabolic partial differential equations. In the category of second-order linear elliptic partial differential equations the form

$$Lu := -\nabla \cdot (K\nabla u - cu) + ru = f \tag{3.2}$$

with $K : \Omega \to \mathbb{R}^{d,d}, c : \Omega \to \mathbb{R}^d$ and $r, f : \Omega \to \mathbb{R}$ is common. Also the parabolic version

$$\frac{\partial u}{\partial t} + Lu = f, \tag{3.3}$$

partial differential equations of first order

$$\nabla \cdot q(u) = 0 \tag{3.4}$$

with nonlinear $q : \mathbb{R} \to \mathbb{R}^d$, partial differential equations of higher order and systems of partial differential equations can be solved numerically with the finite-volume method.

3.1.1 The general idea of the finite-volume method

To deliver insight into the finite-volume method we consider the equation

$$\nabla \cdot q(u) = f. \tag{3.5}$$

The first step of the finite-volume method is to partition the simulation domain Ω. The sub-domains Ω_i have to fulfill the following properties:

- each Ω_i is open, simply connected, and has a polygonal border,

- $\Omega_i \cap \Omega_j = \emptyset$ for $(i \neq j)$,

- $\bigcup_{i=1}^{M} \bar{\Omega}_i = \bar{\Omega}$.

The sub-domains are called control volumes or control areas. The next step is to integrate (3.5) over the control volume Ω_i and use the divergence theorem yielding

$$\int_{\partial \Omega_i} \nu \cdot q(u) d\sigma = \int_{\Omega_i} f dx, \qquad i \in \{1, ..., M\}, \tag{3.6}$$

where ν is the outward pointing normal vector on $\partial \Omega_i$. Because of our requirements, the border $\partial \Omega_i$ consists of n_i lines. So we can write (3.6) as

$$\sum_{j=1}^{n_i} \int_{\Gamma_{ij}} \nu_{ij} \cdot q(u) d\sigma = \int_{\Omega_i} f dx. \tag{3.7}$$

The last step is to discretize the integrals in (3.7). This can be done in various ways.

3.1.2 Example

For our purposes we consider the linear elliptic PDE with homogeneous boundary condition in $\Omega \in \mathbb{R}^2$

$$\begin{aligned}
-\nabla \cdot (k\nabla u - cu) + ru &= f \qquad \text{for } x \in \Omega, \\
u &= 0 \qquad \text{for } x \in \partial \Omega
\end{aligned} \tag{3.8}$$

with $k, r, f : \Omega \to \mathbb{R}$ and $c : \Omega \to \mathbb{R}^2$. For our application we need a two-dimensional grid, but also a Delaunay triangulation or other triangulations are also possible. Integrating both sides yields

$$-\int_{\Omega_i} \nabla \cdot (k\nabla u - cu) dx + \int_{\Omega_i} ru dx = \int_{\Omega_i} f dx \qquad \forall i \in \Lambda, \tag{3.9}$$

where Ω_i is a control volume and Λ is the set of points of our two-dimensional grid. Now we use the divergence theorem and for the first integral we get

$$-\int_{\Omega_i} \nabla \cdot (k\nabla u - cu) dx = -\sum_{j \in \Lambda_i} \int_{\Gamma_{ij}} \nu_{ij} \cdot (k\nabla u - cu) d\sigma, \tag{3.10}$$

where Λ_i are the neighboring points of the node i and ν_{ij} is the outward pointing normal of Γ_{ij}. In the next step we approximate k and $\nu_{ij} \cdot c$ on Γ_{ij} by constants μ_{ij} and γ_{ij} so that the integral becomes

$$-\int_{\Omega_i} \nabla \cdot (k\nabla u - cu)dx \approx -\sum_{j\in\Lambda_i} \int_{\Gamma_{ij}} \mu_{ij}(\nu_{ij} \cdot \nabla u) - \gamma_{ij}ud\sigma. \qquad (3.11)$$

We approximate the normal derivatives by differential quotients, i.e.,

$$\nu_{ij} \cdot \nabla u \approx \frac{u(a_j) - u(a_i)}{d_{ij}} \qquad \text{with } d_{ij} := |a_i - a_j|. \qquad (3.12)$$

For the approximation of the integral of u we use the linear interpolation

$$u|_{\Gamma_{ij}} \approx r_{ij}u(a_i) + (1 - r_{ij})u(a_j) \qquad (3.13)$$

with $r_{ij} \in [0,1]$. The other two integrals are approximated by

$$\int_{\Omega_i} rudx \approx r(a_i)u(a_i)m_i =: r_iu(a_i)m_i$$
$$\int_{\Omega_i} fdx \approx f(a_i)m_i =: f_im_i \qquad (3.14)$$

with $m_i := |\Omega_i|$. In summary we have the system of equations

$$\sum_{j\in\Lambda_i} \left(\mu_{ij}\frac{u_i - u_j}{d_{ij}} + \gamma_{ij}\left(r_{ij}u_i + (1 - r_{ij})u_{ij}\right) \right) m_{ij} + r_iu_im_i = f_im_i, \qquad i \in \Lambda.$$
$$(3.15)$$

3.2 The Scharfetter-Gummel method

We use the Scharfetter-Gummel discretization [8] for the drift-diffusion equations

$$
\begin{aligned}
\nabla \cdot J_n &= R, \\
\nabla \cdot J_p &= -R, \\
J_n &= D_n \nabla n - \mu_n n \nabla V, \\
J_p &= -D_p \nabla p - \mu_p p \nabla V.
\end{aligned}
\tag{3.16}
$$

To discretize the first two equations we use the finite-volume method. Hence we have

$$
\begin{aligned}
m_1\big(J^n_{i+\frac{1}{2},j,k} - J^n_{i-\frac{1}{2},j,k}\big) + m_2\big(J^n_{i,j+\frac{1}{2},k} - J^n_{i,j-\frac{1}{2},k}\big) & \\
+ m_3\big(J^n_{i,j,k+\frac{1}{2}} - J^n_{i,j,k-\frac{1}{2}}\big) &= R(i,j,k) \cdot m, \\
m_1\big(J^p_{i+\frac{1}{2},j,k} - J^p_{i-\frac{1}{2},j,k}\big) + m_2\big(J^p_{i,j+\frac{1}{2},k} - J^p_{i,j-\frac{1}{2},k}\big) & \\
+ m_3\big(J^p_{i,j,k+\frac{1}{2}} - J^p_{i,j,k-\frac{1}{2}}\big) &= -R(i,j,k) \cdot m,
\end{aligned}
\tag{3.17}
$$

where m_1, m_2, and m_3 are the areas of the boundary surfaces of the control volume and m is the volume of the whole control volume. To simplify the following explanations, we rewrite the third and fourth equation in the form

$$
J = -(a\nabla u + bu),
\tag{3.18}
$$

where $a = -D_n$ and $a = D_p$, respectively, $u = n$ and $u = p$, respectively, and $b = \mu_n \nabla V$ and $b = \mu_p \nabla V$, respectively. Now we set $\psi := \frac{b}{a}$ and have

$$
\begin{aligned}
J &= -(a\nabla u + bu) \\
&= -a\nabla u e^{\psi} e^{-\psi} - au\frac{1}{a}be^{\psi}e^{-\psi} \\
&= -ae^{-\psi}(e^{\psi}\partial u + u\partial e^{\psi}) \\
&= -ae^{-\psi}\partial(e^{\psi}u).
\end{aligned}
\tag{3.19}
$$

In the next step we use the assumption that J is constant on every surface of our control volume. Then we have to integrate over the edges of our discretization. To illustrate the method we take the edge between x_i and x_{i+1} and get

$$
-a^{-1}J \int_{x_i}^{x_{i+1}} e^{\psi}dx = \int_{x_i}^{x_{i+1}} \partial(e^{\psi}u) = \delta(e^{\psi}u).
\tag{3.20}
$$

The other edges are analogeous. For the last computation we use linear interpolation for ψ and have

$$\int_{x_i}^{x_{i+1}} e^\psi dx = \left.\frac{e^\psi}{\psi}\right|_{x_i}^{x_{i+1}} \cdot (x_{i+1} - x_i), \tag{3.21}$$

so that we have, for $\psi = -\frac{\mu_n}{D_n}V$ and $\psi = -\frac{\mu_p}{D_p}V$, respectively, the formulas

$$
\begin{aligned}
J^n_{i+\frac{1}{2},j,k} &= -\frac{\mu_n(V_{i+1,j,k} - V_{i,j,k})(e^{c_n V_{i+1,j,k}}n_{i+1,j,k} - e^{c_n V_{i,j,k}}n_{i,j,k})}{(e^{c_n V_{i+1,j,k}} - e^{c_n V_{i,j,k}})(x_{i+1} - x_i)}, \\
J^p_{i+\frac{1}{2},j,k} &= -\frac{\mu_p(V_{i+1,j,k} - V_{i,j,k})(e^{c_p V_{i+1,j,k}}p_{i+1,j,k} - e^{c_p V_{i,j,k}}p_{i,j,k})}{(e^{c_p V_{i+1,j,k}} - e^{c_p V_{i,j,k}})(x_{i+1} - x_i)},
\end{aligned}
\tag{3.22}
$$

where $c_n := -\frac{\mu_n}{D_n}$ and $c_p := \frac{\mu_p}{D_p}$. The formulas for the discretization of the flows in y and in z directions are analogeous. Finally we substitute (3.22) into (3.17) to get the entire discretization.

In the next chapter we will use this method to discretize the model equations.

4 Discretization of the model equations

For the discretization of the model equations we use a 3-dimensional mesh which is equidistant in each coordinate direction. Therefore we use the same axes as in Figure 2.1. We call the distance between two points dx, dy, and dz. Furthermore we call the value of the potential V at the mesh point (i, j, k) $V_{i,j,k}$ and similarly the density of the holes $n_{i,j,k}$, the density of the electrons $p_{i,j,k}$, and the related current flows, $J^n_{i+\frac{1}{2},j,k}$ and $J^p_{i+\frac{1}{2},j,k}$, $J^n_{i,j+\frac{1}{2},k}$ and $J^p_{i,j+\frac{1}{2},k}$, and $J^n_{i,j,k+\frac{1}{2}}$ and $J^p_{i,j,k+\frac{1}{2}}$, respectively. To discretize the whole biosensor we consider each domain separately. The left-hand side of the Poisson equation (2.1) is the same for each domain, and therefore we use the finite-volume method. We have to define a control volume $\Omega_{i,j,k}$ for every mesh point (i, j, k).
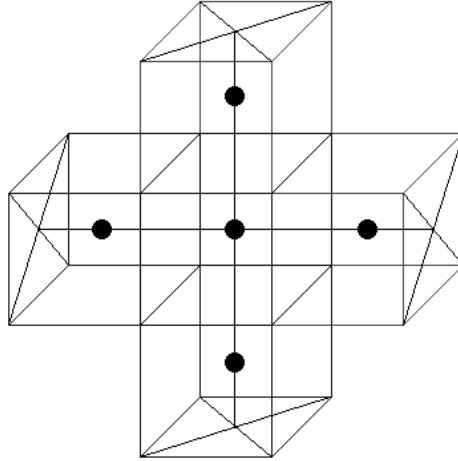
Figure 4.1: Five control volumes with grid points at the centers of the boxes.

Here we use the control volumes

$$\Omega_{i,j,k} := \{x := (x_1, x_2, x_3) \in \Omega : |x_1 - i \cdot dx| \le \frac{dx}{2} \text{ and } |x_2 - j \cdot dy| \le \frac{dy}{2}$$
$$\text{and } |x_3 - k \cdot dz| \le \frac{dz}{2}\}. \tag{4.1}$$

As the next step in the finite-volume method we integrate the Poisson equation over the control volumes and use the divergence theorem to get

$$-\int_{\Omega_{i,j,k}} \nabla \cdot (\varepsilon(x)\nabla V(x)) \, dx = - \sum_{l \in \Lambda_{i,j,k}} \int_{\Gamma_l} \nu_l \varepsilon(x)\nabla V(x) d\sigma, \tag{4.2}$$

where $\Lambda_{i,j,k}$ is the set of the neighbor points of the node (i, j, k), Γ_l is the boundary of the control volume on which the point l is provided and ν_l is the outwards pointing normal on Γ_l (see Figure 4.2).
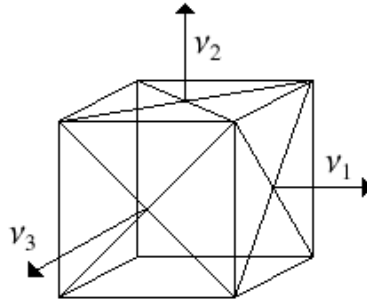
Figure 4.2: A control volume with 3 outward pointing normal vectors.

Now we consider a single neighboring point l and approximate the normal derivative by the differential quotient

$$\nu_l \cdot \nabla V \approx \frac{V_{l_1,l_2,l_3} - V_{i,j,k}}{d}, \tag{4.3}$$

where d is dx, dy or dz depending on the direction where the normal vector ν_l points. To complete the discretization of the left-hand side of the Poisson equation we use our assumption that the permittivity ε is a piecewise constant

function and get

$$\sum_{j\in\Lambda_i}\int_{\Gamma_{ij}}\nu_{ij}\varepsilon(x)\nabla V(x)d\sigma =$$

$$-\left(\varepsilon_{i+\frac{1}{2},j}\frac{V_{i+1,j,k}-V_{i,j,k}}{x_{i+1}-x_i}-\varepsilon_{i-\frac{1}{2},j}\frac{V_{i,j,k}-V_{i-1,j,k}}{x_i-x_{i-1}}\right)\cdot dy\cdot dz$$

$$-\left(\varepsilon_{i,j+\frac{1}{2}}\frac{V_{i,j+1,k}-V_{i,j,k}}{y_{j+1}-y_j}-\varepsilon_{i,j-\frac{1}{2}}\frac{V_{i,j,k}-V_{i,j-1,k}}{y_j-y_{j-1}}\right)\cdot dx\cdot dz$$

$$-\left(\varepsilon_{i,j}\frac{V_{i,j,k+1}-V_{i,j,k}}{z_{k+1}-z_k}-\varepsilon_{i,j}\frac{V_{i,j,k}-V_{i,j,k-1}}{z_k-z_{k-1}}\right)\cdot dx\cdot dy. \tag{4.4}$$

As mentioned before, we now have to consider the different models for the domains to arrive at the discretizations of the right-hand side of equation (2.1). We discuss the discretization in the silicon domain Ω_{Si} first.

4.1 The silicon domain

In the silicon domain Ω_{Si} we have to solve the drift-diffusion equations (2.4). To discretize the electron and hole densities, we use the Scharfetter-Gummel discretization. Hence we have

$$m_1\left(\frac{\mu(V_{i,j,k}-V_{i-1,j,k}(e^{cV_{i,j,k}}u_{i,j,k}-e^{cV_{i-1,j,k}}u_{i-1,j,k})}{(e^{cV_{i,j,k}}-e^{cV_{i-1,j,k}})dx}\right.$$

$$\left.-\frac{\mu(V_{i+1,j,k}-V_{i,j,k}(e^{cV_{i+1,j,k}}u_{i+1,j,k}-e^{cV_{i,j,k}}u_{i,j,k})}{(e^{cV_{i+1,j,k}}-e^{cV_{i,j,k}})dx}\right)$$

$$+m_2\left(\frac{\mu(V_{i,j,k}-V_{i,j-1,k}(e^{cV_{i,j,k}}u_{i,j,k}-e^{cV_{i,j-1,k}}u_{i,j-1,k})}{(e^{cV_{i,j,k}}-e^{cV_{i,j-1,k}})dy}\right.$$

$$\left.-\frac{\mu(V_{i,j+1,k}-V_{i,j,k}(e^{cV_{i,j+1,k}}u_{i,j+1,k}-e^{cV_{i,j,k}}u_{i,j,k})}{(e^{cV_{i,j+1,k}}-e^{cV_{i,j,k}})dy}\right) \tag{4.5}$$

$$+m_3\left(\frac{\mu(V_{i,j,k}-V_{i,j,k-1}(e^{cV_{i,j,k}}u_{i,j,k}-e^{cV_{i,j,k-1}}u_{i,j,k-1})}{(e^{cV_{i,j,k}}-e^{cV_{i,j,k-1}})dz}\right.$$

$$\left.-\frac{\mu(V_{i,j,k+1}-V_{i,j,k}(e^{cV_{i,j,k+1}}u_{i,j,k+1}-e^{cV_{i,j,k}}u_{i,j,k})}{(e^{cV_{i,j,k+1}}-e^{cV_{i,j,k}})dz}\right)$$

$$=\sigma R_{i,j,k}\cdot m,$$

where u stands for n or p and $\sigma = +1$ for $u = n$ and $\sigma = -1$ for $u = p$. Similarly c stands for c_n or c_p and μ for μ_n or μ_p, which are the values from Chapter 3. For the recombination rate we use the Shockley-Read-Hall term with the values

of n and p at the mesh points

$$R_{i,j,k} = \frac{n_{i,j,k}p_{i,j,k} - n_i^2}{\tau_p(n_{i,j,k} + n_i) + \tau_n(p_{i,j,k} + n_i)}. \tag{4.6}$$

Finally we use the finite-volume method for the right-hand side of the Poisson equation. Therefore we integrate the right side over the control volume $\Omega_{i,j,k}$ which was used at the left-hand side and approximate C, n and p to have

$$\int_{\Omega_{i,j,k}} C + n(x) - p(x)dx = (C + n_{i,j,k} - p_{i,j,k}) \cdot m, \tag{4.7}$$

where $n_{i,j,k}$ and $p_{i,j,k}$ are given by the Scharfetter-Gummel discretization, C is the doping concentration and m is again the volume of the control volume $\Omega_{i,j,k}$.

4.2 The liquid and the oxide domain

We discuss the other two domains, the liquid and the oxide, together, because we have to obtain the discretization of the interface conditions where both domains are involved.

4.2.1 The liquid domain

To discretize the right-hand side of the Poisson equation for the liquid we could use

$$\int_{\Omega_i} \sum_{\sigma \in \{-1,1\}} \alpha\sigma f_\sigma e^{-\sigma\beta V(x)} dx = \sum_{\sigma \in \{-1,1\}} \alpha\sigma f_\sigma e^{-\sigma\beta V_{i,j,k}} \cdot m. \tag{4.8}$$

There are two problems, however. First the homogenization method works only for linear operators. Second, this yields a system of nonlinear equations, whereas the following linearization allows us to simplify the problem to a system of linear equations.

4.2.2 Linearization of the Boltzmann term

To linearize the Boltzmann term around V_0 we rewrite it as

$$\sum_{\sigma \in \{-1,1\}} \alpha\sigma e^{-\sigma\beta(V-\Phi)} = \sum_{\sigma \in \{-1,1\}} \alpha\sigma e^{-\sigma\beta(V-V_0)} e^{-\sigma\beta(V_0-\Phi)} \tag{4.9}$$

and replace $e^{-\sigma\beta(V-V_0)}$ by the Taylor series. Hence we get

$$\sum_{\sigma\in\{-1,1\}} \alpha\sigma e^{-\sigma\beta(V-V_0)}e^{-\sigma\beta(V_0-\Phi)} = \sum_{\sigma\in\{-1,1\}} \alpha\sigma e^{-\sigma\beta(V_0-\Phi)}(1 - \sigma\beta(V - V_0) + O(V^2))$$
$$= 2(-\alpha\sinh\beta(V_0 - \Phi) + \alpha\beta V_0\cosh\beta(V_0 - \Phi) - \alpha\beta V\cosh\beta(V_0 - \Phi)). \tag{4.10}$$

For the linearization around $V_0 = 0$ we have

$$\sum_{\sigma\in\{-1,1\}} \alpha\sigma e^{-\sigma\beta(V-\Phi)} \approx 2\alpha(\sinh\beta\Phi - \beta V\cosh\beta\Phi) \tag{4.11}$$

as the Boltzmann term in the discretization.

4.2.3 The oxide domain and the interface conditions

In the oxide, the right-hand side is equal to zero and so we have only to obtain the discretization for the jump conditions

$$V(x+) - V(x-) = \frac{D}{\varepsilon_{Liq}}, \tag{4.12}$$

$$\varepsilon_{Liq}\nabla V(x+) - \varepsilon_{Ox}\nabla V(x-) = -C_s \tag{4.13}$$

at the interface Δ.
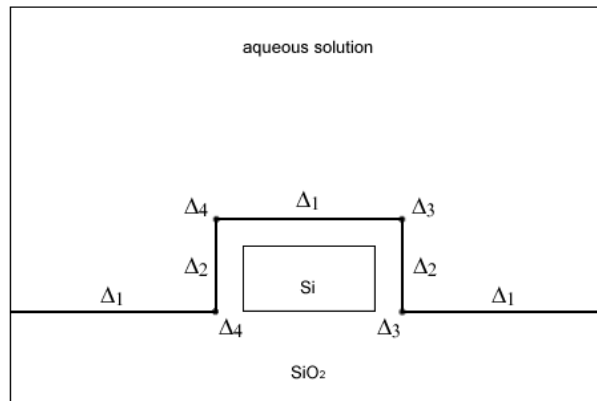
Figure 4.3: The parts of the interface.

Therefore we divide the interface into 4 parts (see Figure 4.3): the horizontal

interface Δ_1, the vertical interface Δ_2, the interface vertices Δ_3 on the right side of the nanowire, and the interface vertices Δ_4 on the left side of the nanowire. We denote the left- and right-hand side limits by substracting and adding $\frac{1}{4}$ in the index. This yields

$$
\begin{aligned}
V_{i,j+\frac{1}{4},k} - V_{i,j-\frac{1}{4},k} &= \frac{D}{\varepsilon_{Liq}}, \\
\varepsilon_{Liq}\frac{V_{i,j+1,k} - V_{i,j+\frac{1}{4},k}}{dy} - \varepsilon_{Ox}\frac{V_{i,j-\frac{1}{4},k} - V_{i,j-1,k}}{dy} &= -C_s,
\end{aligned}
\tag{4.14}
$$

at the interface Δ_1,

$$
\begin{aligned}
V_{i-\frac{1}{4},j,k} - V_{i+\frac{1}{4},j,k} &= \frac{D}{\varepsilon_{Liq}}, \\
\varepsilon_{Liq}\frac{V_{i-1,j,k} - V_{i-\frac{1}{4},j,k}}{dx} - \varepsilon_{Ox}\frac{V_{i+\frac{1}{4},j,k} - V_{i+1,j,k}}{dx} &= -C_s,
\end{aligned}
\tag{4.15}
$$

at the left side of the interface Δ_2,

$$
\begin{aligned}
V_{i+\frac{1}{4},j,k} - V_{i-\frac{1}{4},j,k} &= \frac{D}{\varepsilon_{Liq}}, \\
\varepsilon_{Liq}\frac{V_{i+1,j,k} - V_{i+\frac{1}{4},j,k}}{dx} - \varepsilon_{Ox}\frac{V_{i-\frac{1}{4},j,k} - V_{i-1,j,k}}{dx} &= -C_s,
\end{aligned}
\tag{4.16}
$$

at the right side of the interface Δ_2,

$$
\begin{aligned}
V_{i+\frac{1}{4},j+\frac{1}{4},k} - V_{i-\frac{1}{4},j-\frac{1}{4},k} &= \frac{D}{\varepsilon_{Liq}}, \\
\varepsilon_{Liq}\frac{2(V_{i+1,j+1,k} - V_{i+\frac{1}{4},j+\frac{1}{4},k})}{\sqrt{dx^2 + dy^2}} - \varepsilon_{Ox}\frac{2(V_{i-\frac{1}{4},j-\frac{1}{4},k} - V_{i-1,j-1,k})}{\sqrt{dx^2 + dy^2}} &= -C_s,
\end{aligned}
\tag{4.17}
$$

at the interface Δ_3 and

$$
\begin{aligned}
V_{i-\frac{1}{4},j+\frac{1}{4},k} - V_{i+\frac{1}{4},j-\frac{1}{4},k} &= \frac{D}{\varepsilon_{Liq}}, \\
\varepsilon_{Liq}\frac{2(V_{i-1,j+1,k} - V_{i-\frac{1}{4},j+\frac{1}{4},k})}{\sqrt{dx^2 + dy^2}} - \varepsilon_{Ox}\frac{2(V_{i+\frac{1}{4},j-\frac{1}{4},k} - V_{i+1,j-1,k})}{\sqrt{dx^2 + dy^2}} &= -C_s,
\end{aligned}
\tag{4.18}
$$

at the interface Δ_4. Now we have the discretization for the inner points of the simulation domain and only the boundary conditions are left to complete the discretization.

4.3 The boundary conditions

As mentioned in Chapter 1, we have Dirichlet boundary conditions at the source, drain, and back-gate contacts and at the electrode and Neumann boundary conditions everywhere else. The Dirichlet conditions at the electrode and at the back-gate are

$$
\begin{aligned}
V_{i,0,k} &= V_b, \\
V_{i,yLiq,k} &= V_e
\end{aligned}
\tag{4.19}
$$

for every i and k in our mesh, where V_b and V_e are the same constants as in Chapter 1. The boundary conditions at the source and the drain contacts are

$$
\begin{aligned}
V_{i,j,0} &= V_s + U_T \ln \frac{n_{i,j,0}^D}{n_i}, \\
V_{i,j,zL} &= V_d + U_T \ln \frac{n_{i,j,zL}^D}{n_i}, \\
n_{i,j,0} &= n_{i,j,0}^D, \\
n_{i,j,zL} &= n_{i,j,zL}^D, \\
p_{i,j,0} &= p_{i,j,0}^D, \\
p_{i,j,zL} &= p_{i,j,zL}^D
\end{aligned}
\tag{4.20}
$$

for every i and j in our mesh where

$$
n_{i,j,k}^D = \frac{1}{2}\left(C_{i,j,k} + \sqrt{C_{i,j,k}^2 + 4n_i^2}\right)
$$

and

$$
p_{i,j,k}^D = \frac{1}{2}\left(-C_{i,j,k} + \sqrt{C_{i,j,k}^2 + 4n_i^2}\right)
$$

are the values of the electron and hole densities at the boundary. The Neumann conditions are

$$
\begin{aligned}
V_{xLiq,j,k} &= V_{xLiq-1,j,k}, \\
V_{-xLiq,j,k} &= V_{-xLiq+1,j,k}, \\
V_{i,j,1} &= V_{i,j,2}, \\
V_{i,j,zL} &= V_{i,j,zL-1}
\end{aligned}
\tag{4.21}
$$

for every i, j and k in our mesh and in the silicon domain we have Neumann conditions for the current flow, which are

$$
\begin{aligned}
J^u_{i,ySi+\frac{1}{2},k} &= 0, \\
J^u_{i,yOx1-\frac{1}{2},k} &= 0, \\
J^u_{xSi+\frac{1}{2},j,k} &= 0, \\
J^u_{-xSi-\frac{1}{2},j,k} &= 0
\end{aligned}
\tag{4.22}
$$

for every k in the mesh, $i \in [-x_{Si}, x_{Si}]$ and $j \in [y_{Ox1}, y_{Si}]$, where $u = n$ or $u = p$.

5 Improvements for 3D simulations

We developed two improvements for the discretization in Chapter 3. The first change is that we halve the number of grid points by using the symmetry of the biosensor. The second improvement is needed because we have to implement the interface conditions efficiently on an equidistant grid.

5.1 Exploiting the symmetry

A quick look on Figure 1.1 is enough to understand the symmetry of the biosensor and the idea is obvious that we reflect the biosensor about the y-axis. The advantage of this reflection is that we only need a bit more than half of the points and so the computation is much faster. To get the right conditions for the points on the y-axis we only have to set

$$
\begin{aligned}
V_{-1,j,k} &:= V_{1,j,k} \\
n_{-1,j,k} &:= n_{1,j,k} \\
p_{-1,j,k} &:= p_{1,j,k}
\end{aligned}
\tag{5.1}
$$

for every index j and k on the grid. As a consequence we can limit the following explanations to points with $x \geq 0$.

5.2 Efficient implementation of the interface conditions

In Chapter 3 we started with an equidistant grid, but we need additional grid points for the interface conditions. For instance at the interface Δ_1, we call the two limits $V_{i,j+\frac{1}{4},k}$ and $V_{i,j-\frac{1}{4},k}$. The idea is now to use the points $V_{i,j,k}$ and $V_{i,j-1,k}$ instead of the points $V_{i,j+\frac{1}{4},k}$ and $V_{i,j-\frac{1}{4},k}$. This can be done similarly for

the points at the interface Δ_2. So we have the equations

$$V_{i,j,k} - V_{i,j-1,k} = \frac{D}{\varepsilon_{Liq}},$$

$$\varepsilon_{Liq} \frac{V_{i,j+1,k} - V_{i,j,k}}{dy} - \varepsilon_{Ox} \frac{V_{i,j-1,k} - V_{i,j-2,k}}{dy} = -C_s \tag{5.2}$$

at the interface Δ_1 and

$$V_{i,j,k} - V_{i-1,j,k} = \frac{D}{\varepsilon_{Liq}},$$

$$\varepsilon_{Liq} \frac{V_{i+1,j,k} - V_{i,j,k}}{dx} - \varepsilon_{Ox} \frac{V_{i-1,j,k} - V_{i-2,j,k}}{dx} = -C_s, \tag{5.3}$$

at the interface Δ_2.
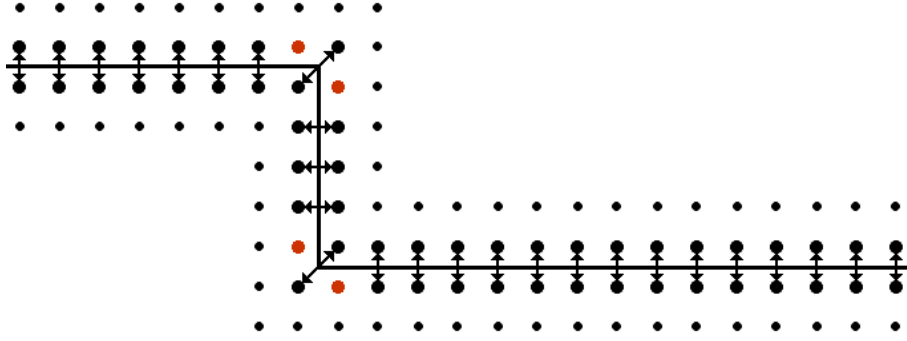
Figure 5.1: Linking of the grid points at the interface. The red points are additional points which are treated in Figure 5.2.

At the interface Δ_3 we have the equations

$$V_{i,j,k} - V_{i-1,j-1,k} = \frac{D}{\varepsilon_{Liq}},$$

$$\varepsilon_{Liq} \frac{2(V_{i+1,j+1,k} - V_{i,j,k})}{\sqrt{dx^2 + dy^2}} - \varepsilon_{Ox} \frac{2(V_{i-1,j-1,k} - V_{i-2,j-2,k})}{\sqrt{dx^2 + dy^2}} = -C_s. \tag{5.4}$$

But now we have the problem that we have additional points at $(x_{Ox} - 1, j, k)$ where $(j, k) \in [y_{Ox2}, y_{Liq} - 1] \times [1, L_z - 1]$, $(i, y_{Ox2} - 1, k)$ where $(i, k) \in [x_{Ox}, x_{Liq} - 1] \times [1, L_z - 1]$, (i, y_{Ox1}, k) where $(i, k) \in [0, x_{Ox} - 1] \times [1, L_z - 1]$, and (x_{Ox}, j, k) where $(j, k) \in [1, y_{Ox1} - 1] \times [1, L_z - 1]$ which are shown in Figure 5.2 as red points. These points does not exist in our original discretization, so we combine

these points with points nearby. First we identify them with existing points by adding the equations

$$
\begin{aligned}
V_{x_{Ox}-1,j,k} &= V_{x_{Ox},j,k} & \text{for } (j,k) \in ([1, y_{Ox1}-1] \cup [y_{Ox2}, y_{Liq}-1]) \times [1, L_z-1], \\
V_{i,y_{Ox2},k} &= V_{i,y_{Ox2}-1,k} & \text{for } (i,k) \in [x_{Ox}, x_{Liq}-1] \times [1, L_z-1], \\
V_{i,y_{Ox1},k} &= V_{i,y_{Ox1}-1,k} & \text{for } (i,k) \in [0, x_{Ox}-1] \times [1, L_z-1]
\end{aligned}
$$
(5.5)

and then we have to connect the points in the original grid via the Poisson equation

$$
\begin{aligned}
-&\left(\varepsilon_{i+\frac{1}{2},j} \frac{V_{i+1,j,k}-V_{i,j,k}}{dx} - \varepsilon_{i-\frac{3}{2},j} \frac{V_{i,j,k}-V_{i-2,j,k}}{dx} \right) \cdot dy \cdot dz \\
-&\left(\varepsilon_{i,j+\frac{1}{2}} \frac{V_{i,j+1,k}-V_{i,j,k}}{dy} - \varepsilon_{i,j-\frac{1}{2}} \frac{V_{i,j,k}-V_{i,j-1,k}}{dy} \right) \cdot dx \cdot dz \\
-&\left(\varepsilon_{i,j} \frac{V_{i,j,k+1}-V_{i,j,k}}{dz} - \varepsilon_{i,j} \frac{V_{i,j,k}-V_{i,j,k-1}}{dz} \right) \cdot dx \cdot dy = rhs
\end{aligned}
$$
(5.6)
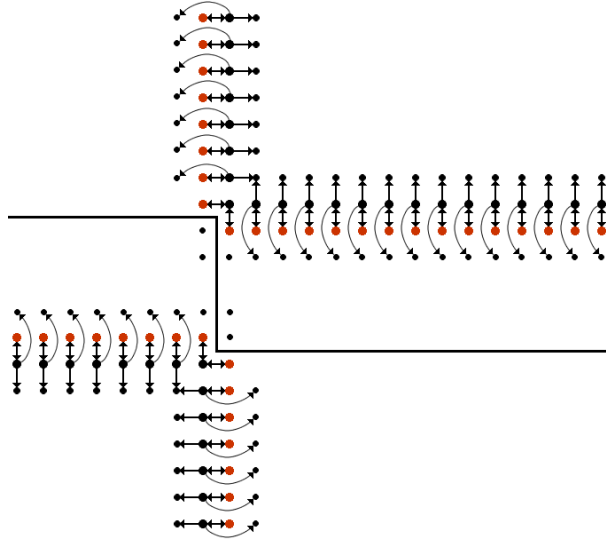
Figure 5.2: The red points are additional points which identified with black points. The other arrows show the points which are affected by the Poisson equation.

at the points $i = x_{Ox}$ and $(j,k) \in [y_{Ox2}+1, y_{Liq}-1] \times [1, zL-1]$, via the equations

$$-\left(\varepsilon_{i+\frac{3}{2},j}\frac{V_{i+2,j,k}-V_{i,j,k}}{dx}-\varepsilon_{i-\frac{1}{2},j}\frac{V_{i,j,k}-V_{i-1,j,k}}{dx}\right)\cdot dy\cdot dz$$

$$-\left(\varepsilon_{i,j+\frac{1}{2}}\frac{V_{i,j+1,k}-V_{i,j,k}}{dy}-\varepsilon_{i,j-\frac{1}{2}}\frac{V_{i,j,k}-V_{i,j-1,k}}{dy}\right)\cdot dx\cdot dz \qquad (5.7)$$

$$-\left(\varepsilon_{i,j}\frac{V_{i,j,k+1}-V_{i,j,k}}{dz}-\varepsilon_{i,j}\frac{V_{i,j,k}-V_{i,j,k-1}}{dz}\right)\cdot dx\cdot dy = rhs$$

at the points $i = x_{Ox}$ and $(j,k) \in [1, y_{Ox1} - 2] \times [1, zL - 1]$, via the equations

$$-\left(\varepsilon_{i+\frac{1}{2},j}\frac{V_{i+1,j,k}-V_{i,j,k}}{dx}-\varepsilon_{i-\frac{1}{2},j}\frac{V_{i,j,k}-V_{i-1,j,k}}{dx}\right)\cdot dy\cdot dz$$

$$-\left(\varepsilon_{i,j+\frac{1}{2}}\frac{V_{i,j+1,k}-V_{i,j,k}}{dy}-\varepsilon_{i,j-\frac{3}{2}}\frac{V_{i,j,k}-V_{i,j-2,k}}{dy}\right)\cdot dx\cdot dz \qquad (5.8)$$

$$-\left(\varepsilon_{i,j}\frac{V_{i,j,k+1}-V_{i,j,k}}{dz}-\varepsilon_{i,j}\frac{V_{i,j,k}-V_{i,j,k-1}}{dz}\right)\cdot dx\cdot dy = rhs$$

at the points $j = y_{Ox2}$ and $(i,k) \in [x_{Ox} + 1, x_{Liq} - 1] \times [1, zL - 1]$, and finally via the equations

$$-\left(\varepsilon_{i+\frac{1}{2},j}\frac{V_{i+1,j,k}-V_{i,j,k}}{dx}-\varepsilon_{i-\frac{1}{2},j}\frac{V_{i,j,k}-V_{i-1,j,k}}{dx}\right)\cdot dy\cdot dz$$

$$-\left(\varepsilon_{i,j+\frac{3}{2}}\frac{V_{i,j+2,k}-V_{i,j,k}}{dy}-\varepsilon_{i,j-\frac{1}{2}}\frac{V_{i,j,k}-V_{i,j-1,k}}{dy}\right)\cdot dx\cdot dz \qquad (5.9)$$

$$-\left(\varepsilon_{i,j}\frac{V_{i,j,k+1}-V_{i,j,k}}{dz}-\varepsilon_{i,j}\frac{V_{i,j,k}-V_{i,j,k-1}}{dz}\right)\cdot dx\cdot dy = rhs$$

at the points $j = y_{Ox1} - 1$ and $(i,k) \in [0, x_{Ox} - 2] \times [1, zL - 1]$. Here rhs stands for the right-hand side of the respective Poisson equation.

5.3 Matrix structure

After these improvements the linear system has the structure shown in Figure 5.3, which is similar to the usual band structure of discretizations of the Poisson equation.
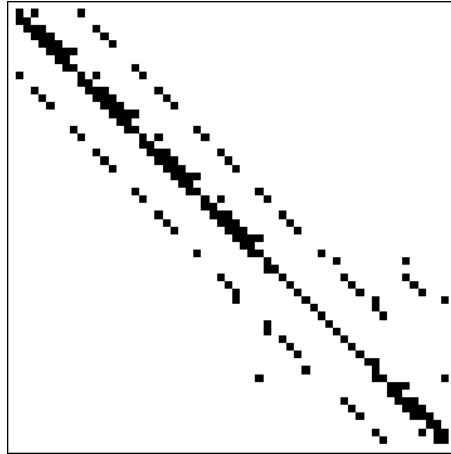
Figure 5.3: Structure of the linear system.

It also shows that there are non-zero points which are not in the usual band structure. These points are the equations for the vertical interface Δ_2. Because of the small parameters used in the simulation shown in Figure 5.3, not all of the 7 bands of the discretization of the 3D Poisson equation are seen.
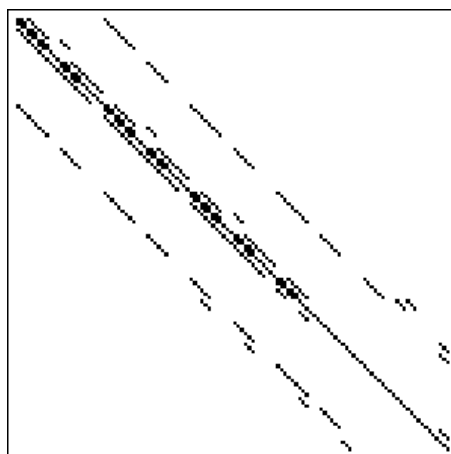
Figure 5.4: Structure of the linear system with larger parameters.

In Figure 5.4 larger parameters are used and the 7-band structure is clearly seen. It is also observed in Figure 5.4 that the band structure of the equations with the interface conditions is not worse than the band structure of the discretization of the 3D Poisson equation. This means that our implementation works very efficiently.

6 The program

Listing 6.1 shows the Mathematica program in pseudo code where we use a stepping method for the boundary conditions to improve convergence. In Listing 6.1 we use as example the boundary conditions at the back-gate and the source.

Listing 6.1: Numerical algorithm.

```
1  for(i=0,i<iterB,i++){
2    Vb=startB+i*stepB
3    for(j=0,j<iterS,j++){
4      Vs=startS+j*stepS
5      if(i==0 && j==0){ n[0]=p[0]=0 }
6      else if{i>0 && j==0){
7        n[0]=soln[i-1,j]
8        p[0]=solp[i-1,j]
9      }
10     else{
11       n[0]=soln[i,j-1]
12       p[0]=solp[i,j-1]
13     }
14
15     k = V[0] = 0
16
17     while(k<maxIterations){
18        V[k+1] = B(n[k],p[k])
19        n[k+1] = N(V[k+1],n[k],p[k])
20        p[k+1] = N(V[k+1],n[k+1],p[k+1])
21        deltaV = ||V[k+1] - V[k]||
22
23        if(deltaV < maxDelta) : break
24        k++
25     }
26     soln[i,j] = n[k]
27     solp[i,j] = p[k]
28     solV[i,j] = V[k]
29   }
30 }
```

Here we compute n and p with the Newton method and V with the Bi-CGSTAB method which is a Krylov method. For more details to the Newton method and the Bi-CGSTAB method see [1, 7, 14].

This schematic program will start with the boundary conditions $V_b = startB$ and $V_s = startS$ and will make $iterB$ steps with step size $stepB$ for the back-gate and $iterS$ steps with step size $stepS$ for the source contact. The setting of the start values of n and p provides a better approximation in the loop where $k = 0$. Furthermore we use the infinity norm for the computation of $deltaV$ and the tolerance limit $maxDelta := 10^{-6}$V.

7 Simulation and numerical results

For the simulations shown in this chapter we consider a leading example. The parameters of the reference structure are shown in Table 7.1.

$$
\begin{array}{lll}
dx = 1 & dy = 1 & dz = 1 \\
x_{Si} = 9\text{nm} & y_{Ox1} = 9\text{nm} & L_z = 19\text{nm} \\
x_{Ox} = 12\text{nm} & y_{Si} = 17\text{nm} & \\
x_{Liq} = 24\text{nm} & y_{Ox2} = 20\text{nm} & \\
& y_{Liq} = 34\text{nm} &
\end{array}
$$

Table 7.1: The length scales of the example.

If not noted otherwise, the values of Table 7.2 will be used.

$$
\begin{array}{lll}
\Phi = 0 & C_s = -2 \cdot 10^{-19}\text{q} \cdot \text{nm}^{-2} & \alpha = 6.02214 \cdot 10^{-5}\text{mole} \cdot \text{nm}^{-3} \\
C = 10^{-5}\text{q} \cdot \text{nm}^{-3} & D = 0\text{q} \cdot \text{nm}^{-2} &
\end{array}
$$

Table 7.2: Basic setting.

In the following we will often compute the current I_{SD} between source and drain. It is computed by the formula

$$
I_{SD} = \sum_{i=-x_{Si}}^{x_{Si}} \sum_{j=y_{Ox1}+1}^{y_{Si}} \left(J^p_{i,j,k-\frac{1}{2}} + J^n_{i,j,k-\frac{1}{2}} \right), \tag{7.1}
$$

where k is an integer in $[2, L_z - 1]$.

7.1 Boundary conditions

In this paragraph we discuss the hole density p, the electron density n, and the electric potential V for varying boundary conditions. Therefore we use different cross sections in the plots. The cross sections in x and y-directions are shown in Figure 7.1.
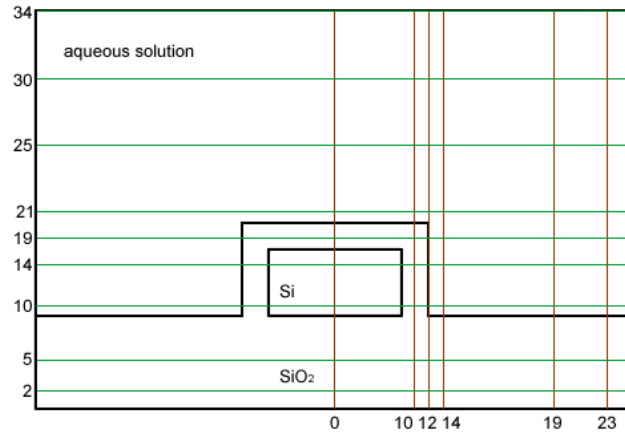
Figure 7.1: Cross sections shown in simulations.

Furthermore the current I_{SD} for varying boundary conditions is summarized in Table 7.3. We chose the parameters in Table 7.3 to investigate the influence of the different boundary conditions separately and some of their interactions.

Settings								I_{SD} [A]
$V_b =$	0V,	$V_e =$	0V,	$V_s =$	0V,	$V_d = 0V$		$5.93208 \cdot 10^{-23}$
$V_b =$	$-3V$,	$V_e =$	0V,	$V_s =$	0V,	$V_d = 0V$		$9.85995 \cdot 10^{-28}$
$V_b =$	0V,	$V_e =$	$-1V$,	$V_s =$	0V,	$V_d = 0V$		$-1.12338 \cdot 10^{-26}$
$V_b =$	0V,	$V_e =$	0V,	$V_s =$	5V,	$V_d = 0V$		$1.43795 \cdot 10^{-6}$
$V_b =$	0V,	$V_e =$	0V,	$V_s =$	0V,	$V_d = 5V$		$-1.43795 \cdot 10^{-6}$
$V_b =$	0V,	$V_e =$	0V,	$V_s =$	$-5V$,	$V_d = 5V$		$-33.3354 \cdot 10^{-6}$
$V_b =$	$-2V$,	$V_e =$	1V,	$V_s =$	0V,	$V_d = 0V$		$4.13576 \cdot 10^{-22}$
$V_b =$	$-2.5V$,	$V_e =$	2.5V,	$V_s =$	$-5V$,	$V_d = 5V$		$-40.3515 \cdot 10^{-6}$

Table 7.3: Current for varying boundary conditions.

Results for $V_b = 0$V, $V_e = 0$V, $V_s = 0$V, $V_d = 0$V

Figure 7.2 shows the electric potential in cross sections in x-direction. The three cross sections at the top (always from left to right) are for the values $x = 0$nm, $x = 10$nm, and $x = 12$nm and the three cross sections at the bottom are for the values $x = 14$nm, $x = 19$nm, and $x = 23$nm. The common of all six pictures are that we see the boundary condition for the back-gate at the left side of the pictures and the boundary condition for the electrode at the right side of the pictures. In the three figures at the top we see how the semiconductor (from $y = 9$nm to $y = 17$nm) influences the electric potential V and that the boundary conditions at the source and the drain for the Ohmic contacts depend not only on the applied voltage, see (2.11). The three pictures at the bottom show the results at the surface with zero-flux boundary conditions at the left- and on the right-hand side (at $x = -24$nm and $x = 24$nm) of the biosensor in contrast to Dirichlet boundary conditions.
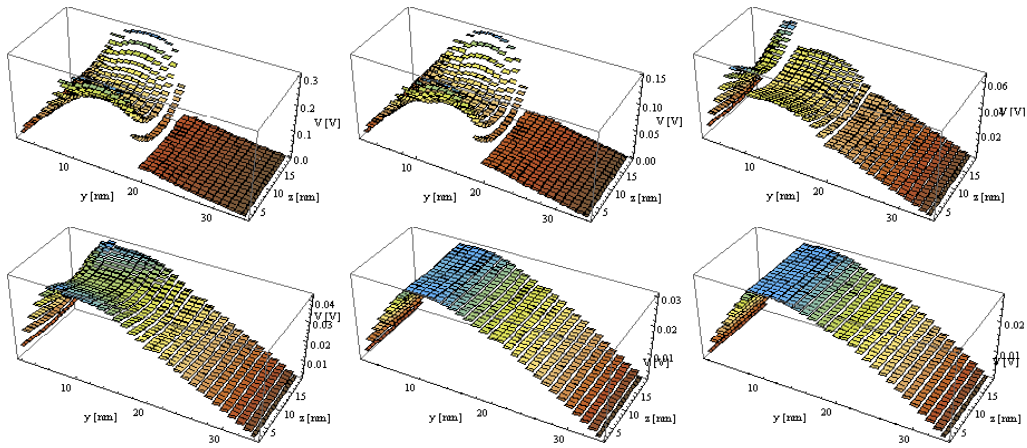

Figure 7.2: Cross sections at $x = 0$nm, $x = 10$nm, $x = 12$nm, $x = 14$nm, $x = 19$ nm, and $x = 23$nm showing the electric potential V.

The cross sections at $z = 5$nm, $z = 10$nm, and $z = 15$nm are shown in Figure 7.3 where the semiconductor part from $x = -9$nm to $x = 9$nm and from $y = 9$nm to $y = 17$nm is clearly seen.

Figure 7.4 shows the cross sections (from left to right and top to bottom) at $y = 2$nm, $y = 5$nm, $y = 10$nm, $y = 14$nm, $y = 19$nm, $y = 21$nm, $y = 25$nm, $y = 30$nm, and $y = 34$nm. Here we see again the influence of the semiconductor (from $x = -9$nm to $x = 9$nm) on the electric potential V.

Figure 7.5, Figure 7.6, and Figure 7.7 shows cross sections for the electron density

n and the hole density p. The hole density p will be always very small because we have a n-doped nanowire and hence the electrons are the major carriers. The following paragraphs show the same cross sections for varying boundary conditions.
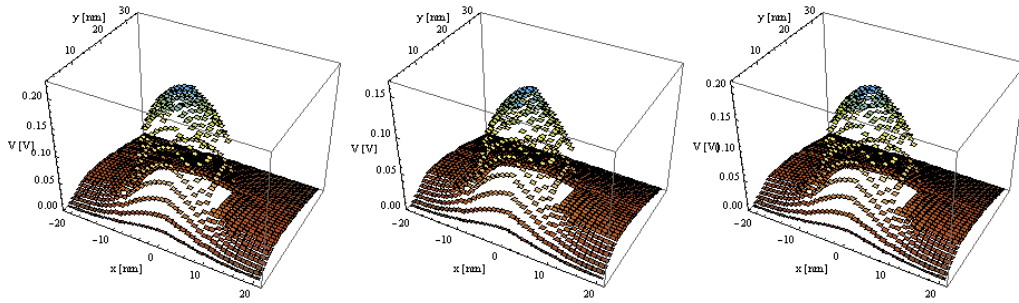

Figure 7.3: Cross sections at $z = 5$nm, $z = 10$nm, and $z = 15$nm showing the electric potential V.
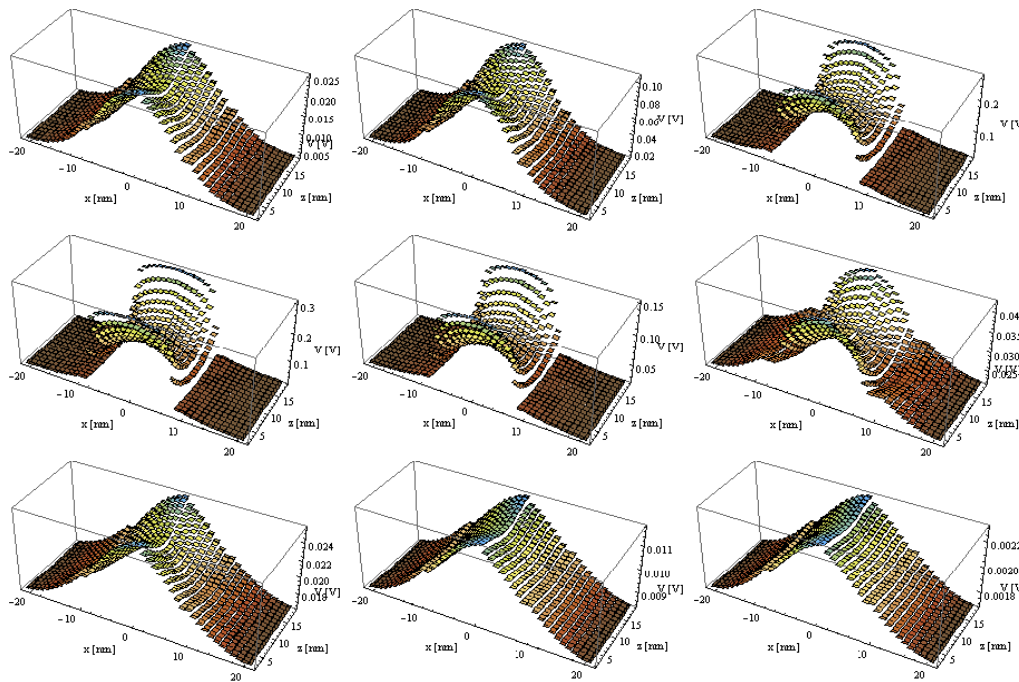
Figure 7.4: Cross sections at $y = 2$nm, $y = 5$nm, $y = 10$nm, $y = 14$nm, $y = 19$nm, $y = 21$nm, $y = 25$nm, $y = 30$nm, and $y = 34$nm showing the electric potential V.
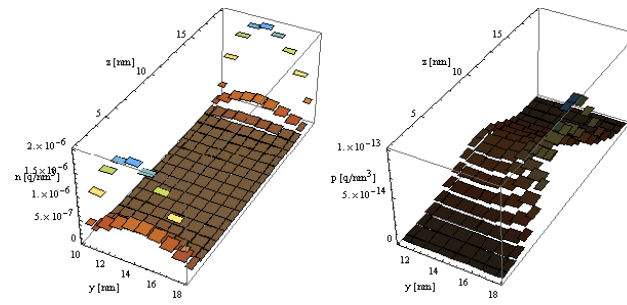
Figure 7.5: Cross sections at $x = 5$nm showing the electron density n and the hole density p.
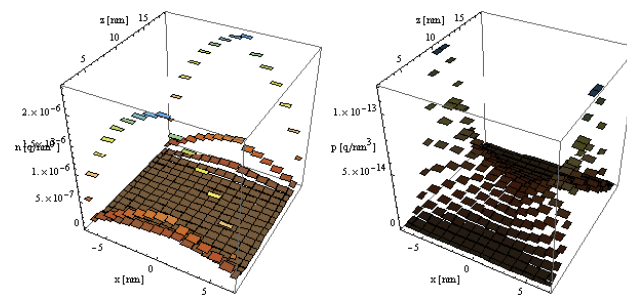
Figure 7.6: Cross sections at $y = 14$nm showing the electron density n and the hole density p.
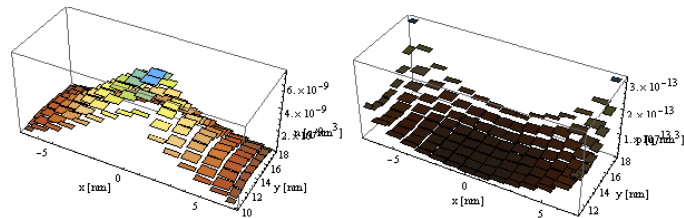
Figure 7.7: Cross sections at $z = 10$nm showing the electron density n and the hole density p.

Results for $V_b = -3\text{V}$, $V_e = 0\text{V}$, $V_s = 0\text{V}$, $V_d = 0\text{V}$

Figure 7.8 shows the effect of the boundary condition at the back-gate which we
can see at the left side of the pictures.
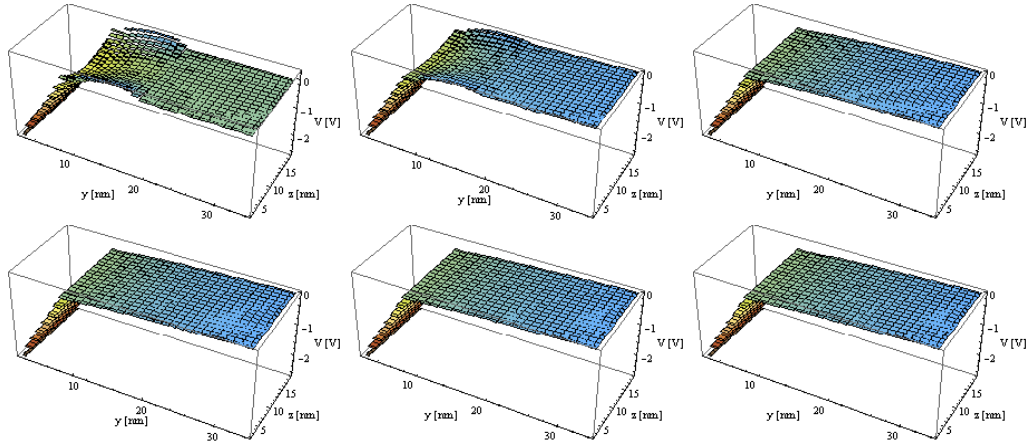
Figure 7.8: Cross sections at $x = 0$nm, $x = 10$nm, $x = 12$nm, $x = 14$nm, $x = 19$
nm, and $x = 23$nm showing the electric potential V.

In Figure 7.9 we see the same effect as in Figure 7.8. Hence we have a decrease
of the electric potential in direction to the bulk.

The same effect as in Figure 7.8 is seen in the first three pictures of Figure
7.10. In the other pictures we see no effect.

In Figure 7.12 we have a increase of the hole density p. We have this effect
if we have less current I_{SD}.
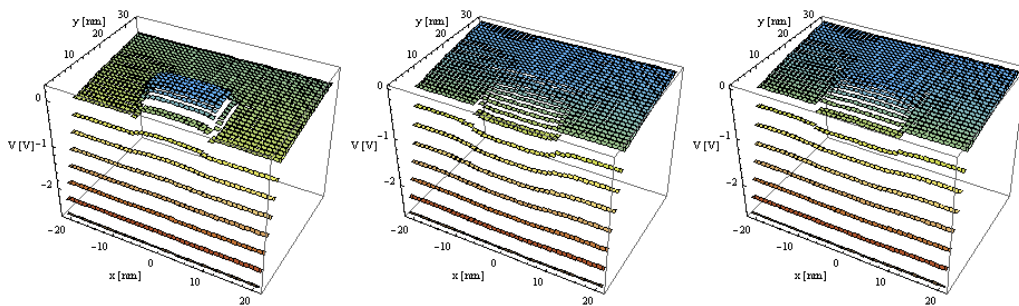
Figure 7.9: Cross sections at $z = 5$nm, $z = 10$nm, and $z = 15$nm showing the
electric potential V.
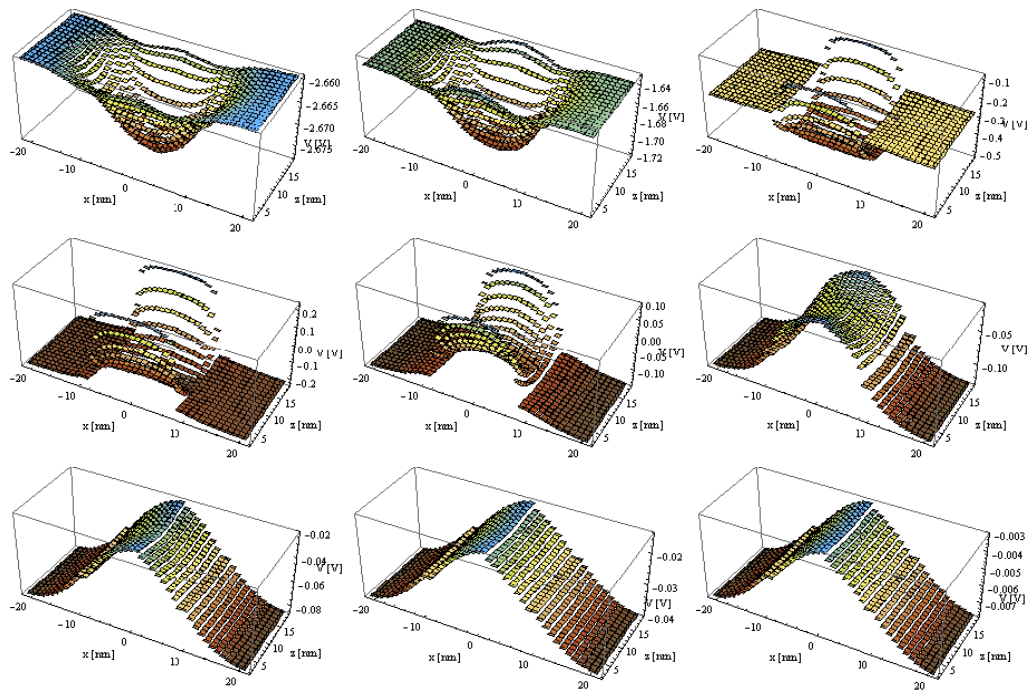
Figure 7.10: Cross sections at $y = 2$nm, $y = 5$nm, $y = 10$nm, $y = 14$nm, $y = 19$nm, $y = 21$nm, $y = 25$nm, $y = 30$nm, and $y = 34$nm showing the electric potential V.
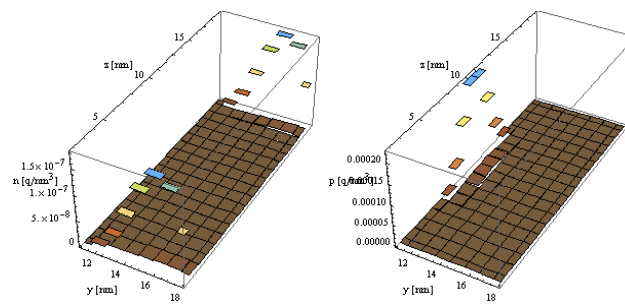

Figure 7.11: Cross sections at $x = 5$nm showing the electron density n and the hole density p.
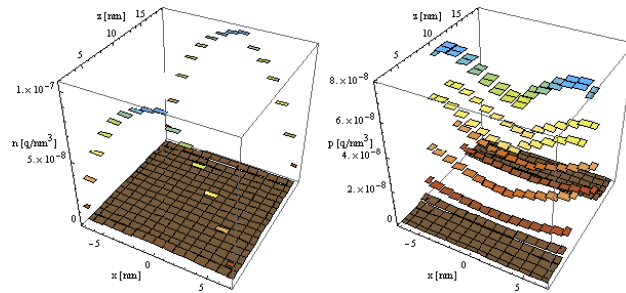
Figure 7.12: Cross sections at $y = 14$nm showing the electron density n and the hole density p.
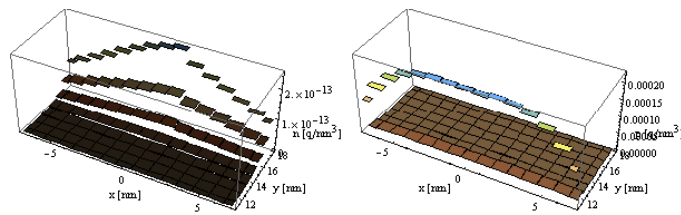
Figure 7.13: Cross sections at $z = 10$nm showing the electron density n and the hole density p.

Results for $V_b = 0$V, $V_e = -1$V, $V_s = 0$V, $V_d = 0$V

Figure 7.14 shows the influence of the boundary condition at the electrode at the right side of the pictures.
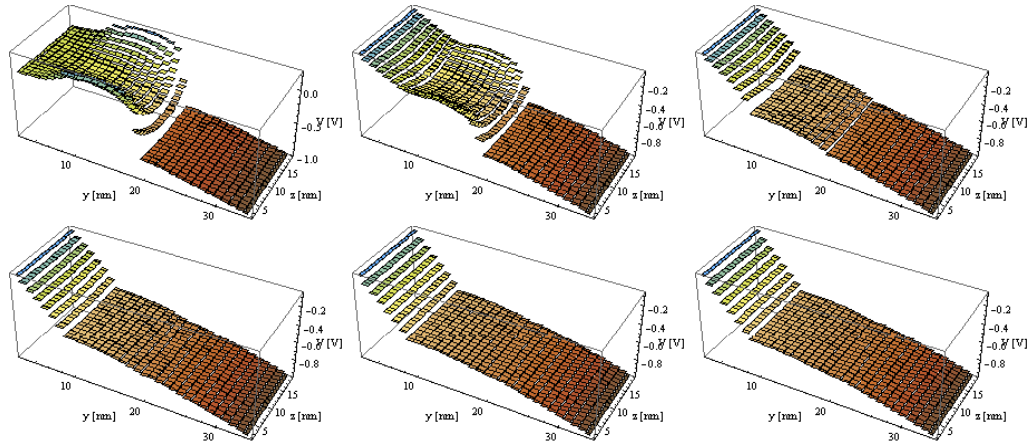

Figure 7.14: Cross sections at $x = 0$nm, $x = 10$nm, $x = 12$nm, $x = 14$nm, $x = 19$ nm, and $x = 23$nm showing the electric potential V.

Figure 7.15 shows an decrease of the potential in direction to the electrode.

The first 5 pictures of Figure 7.16 are not influenced by the electrode boundary condition. In the other pictures we see a decrease of the average electric potential V.

The hole density p and the electron density n are as expected.
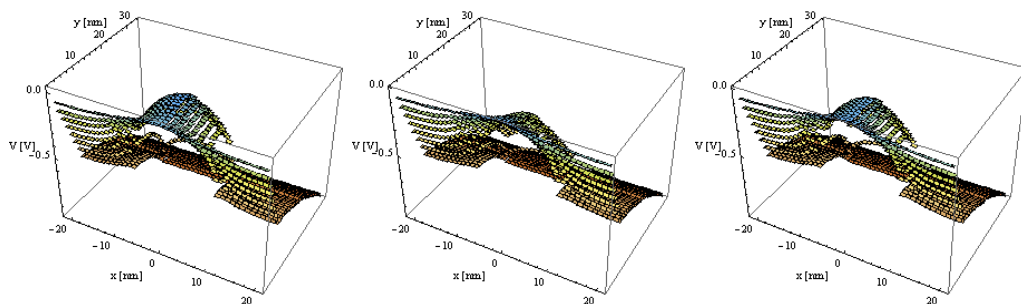
Figure 7.15: Cross sections at $z = 5$nm, $z = 10$nm, and $z = 15$nm showing the electric potential V.
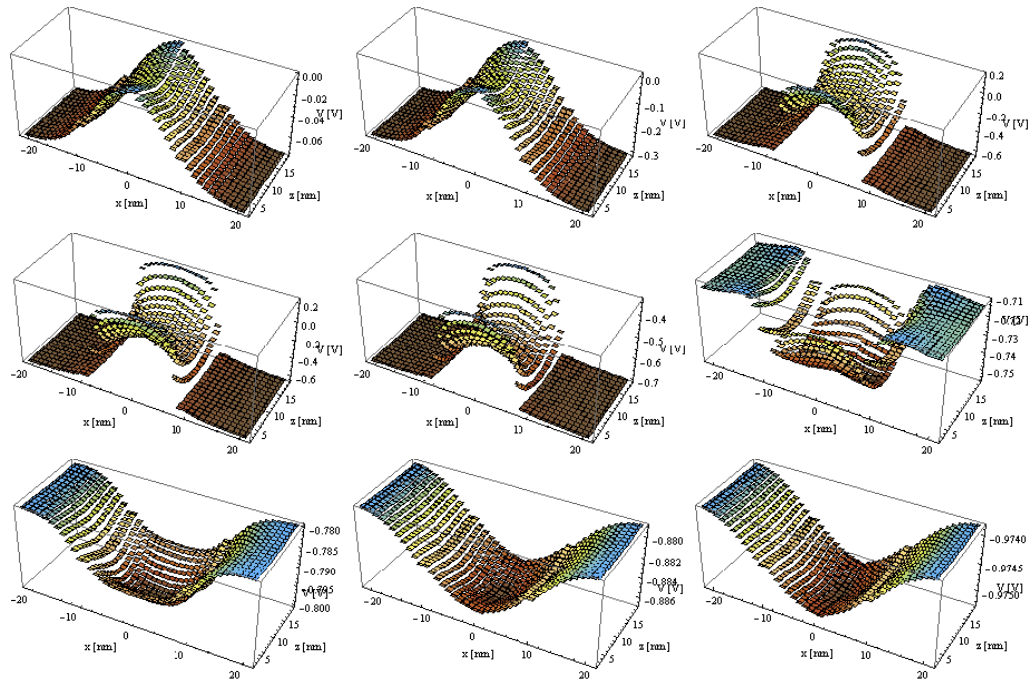
Figure 7.16: Cross sections at $y = 2$nm, $y = 5$nm, $y = 10$nm, $y = 14$nm, $y = 19$nm, $y = 21$nm, $y = 25$nm, $y = 30$nm, and $y = 34$nm showing the electric potential V.
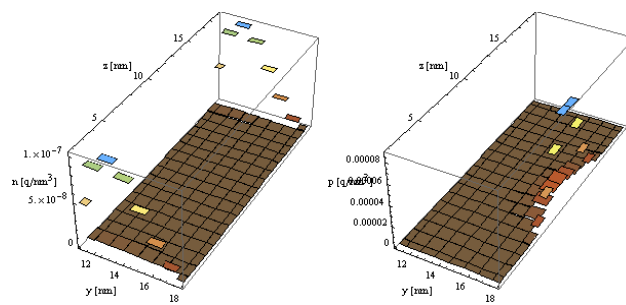

Figure 7.17: Cross sections at $x = 5$nm showing the electron density n and the hole density p.
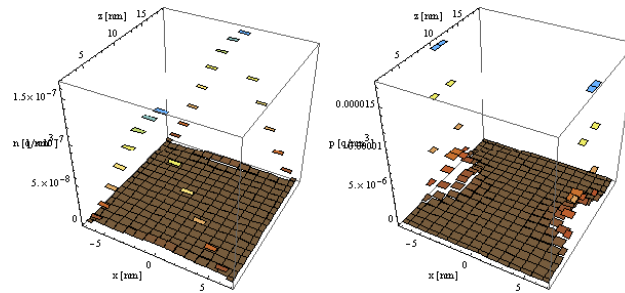
Figure 7.18: Cross sections at $y = 14$nm showing the electron density n and the hole density p.
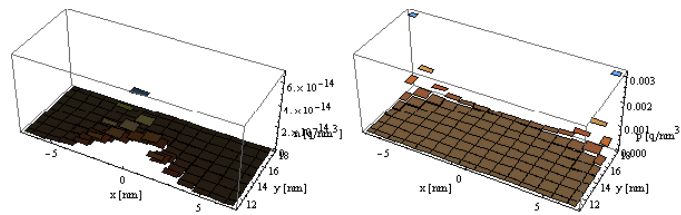
Figure 7.19: Cross sections at $z = 10$nm showing the electron density n and the hole density p.

Results for $V_b = 0$V, $V_e = 0$V, $V_s = 5$V, $V_d = 0$V

Figure 7.20 shows an increase of the electric potential V in the silicon domain at the source and nearby.
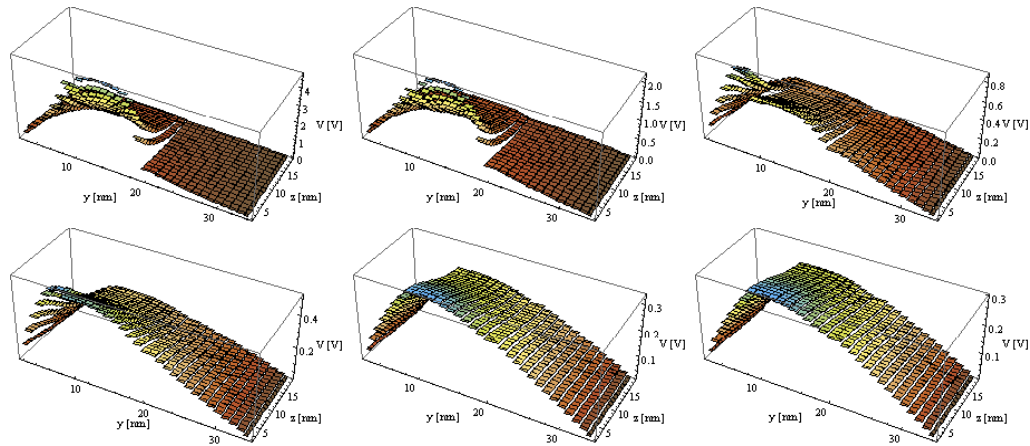

Figure 7.20: Cross sections at $x = 0$nm, $x = 10$nm, $x = 12$nm, $x = 14$nm, $x = 19$ nm, and $x = 23$nm showing the electric potential V.

In Figure 7.21 we have on the first picture an increase of the average electric potential V.

Figure 7.22 is clearly influenced from the boundary condition at the source. This results in an increase of the electric potential V at the source.

Since we have a n-doped nanowire only the density of the electrons at the source increases in Figure 7.23, 7.24, and 7.25.
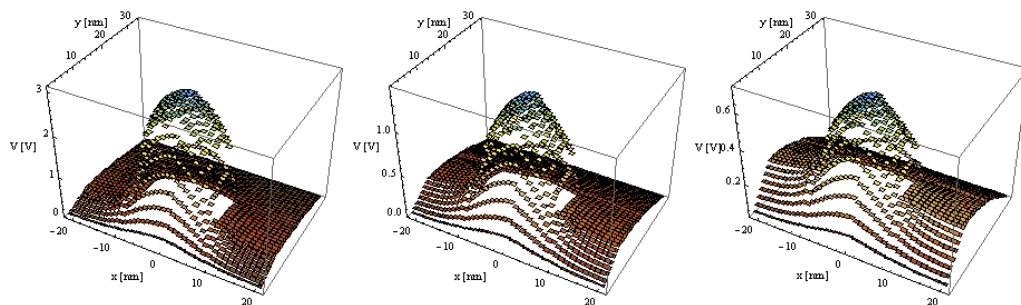

Figure 7.21: Cross sections at $z = 5$nm, $z = 10$nm, and $z = 15$nm showing the electric potential V.
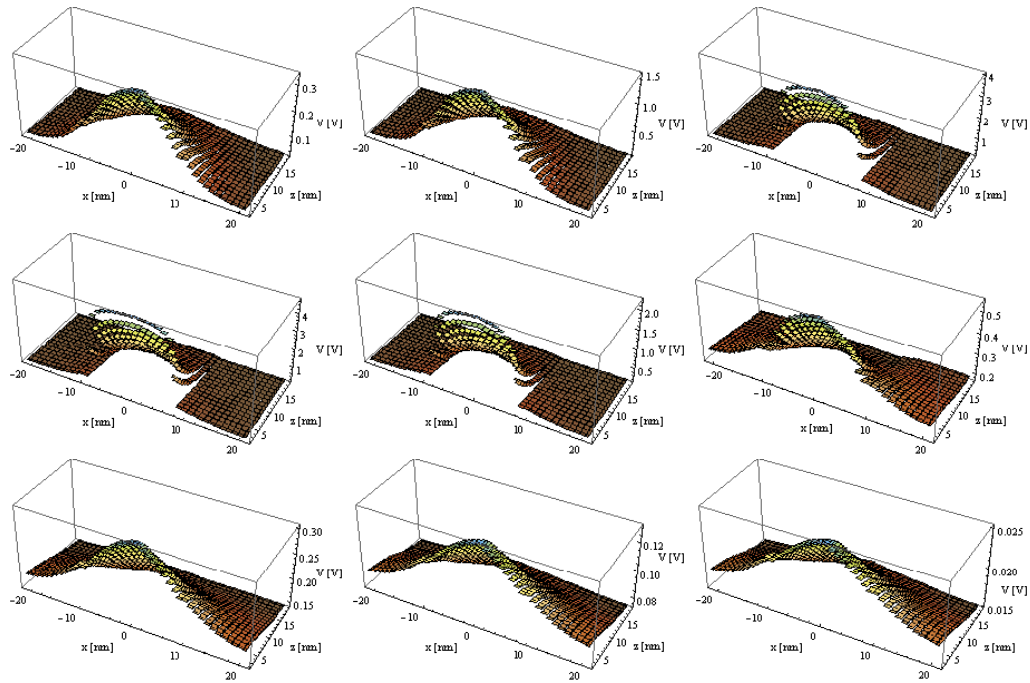
Figure 7.22: Cross sections at $y = 2$nm, $y = 5$nm, $y = 10$nm, $y = 14$nm, $y = 19$nm, $y = 21$nm, $y = 25$nm, $y = 30$nm, and $y = 34$nm showing the electric potential V.
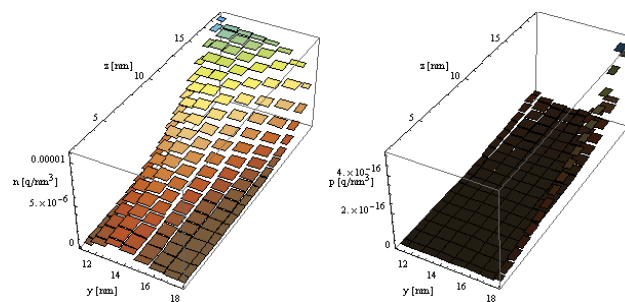
Figure 7.23: Cross sections at $x = 5$nm showing the electron density n and the hole density p.
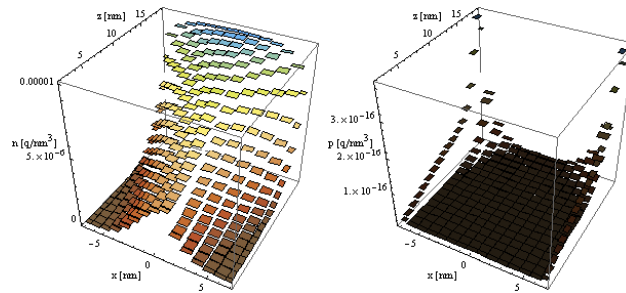
Figure 7.24: Cross sections at $y = 14$nm showing the electron density n and the hole density p.
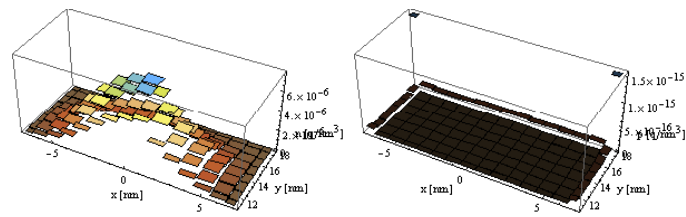
Figure 7.25: Cross sections at $z = 10$nm showing the electron density n and the hole density p.

Results for $V_b = 0\text{V}$, $V_e = 0\text{V}$, $V_s = 0\text{V}$, $V_d = 5\text{V}$

Here we can see the same effect as in the previous paragraph. The difference is the direction of the increasing electric potential V.
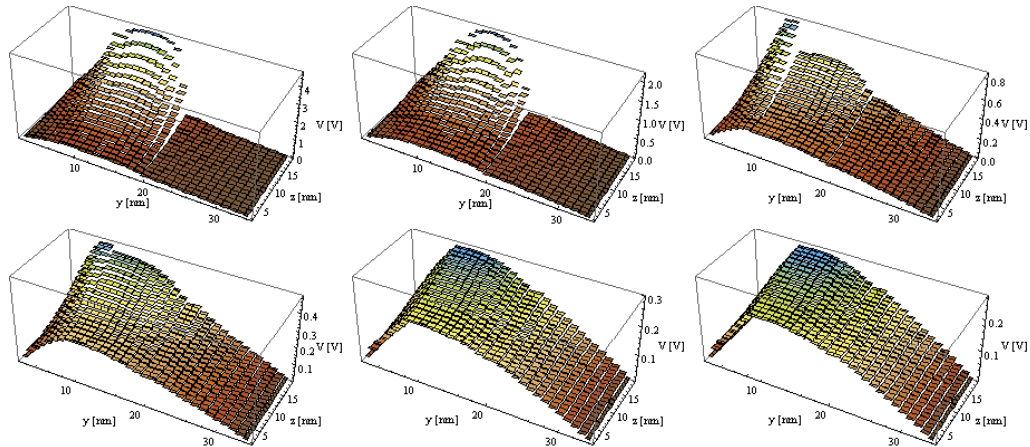
Figure 7.26: Cross sections at $x = 0$nm, $x = 10$nm, $x = 12$nm, $x = 14$nm, $x = 19$ nm, and $x = 23$nm showing the electric potential V.
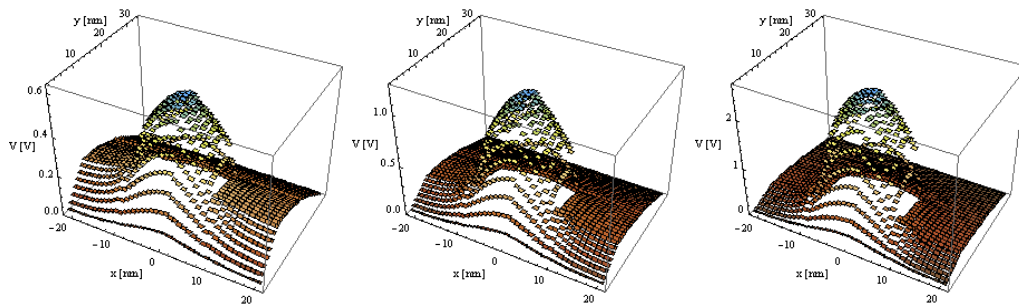
Figure 7.27: Cross sections at $z = 5$nm, $z = 10$nm, and $z = 15$nm showing the electric potential V.
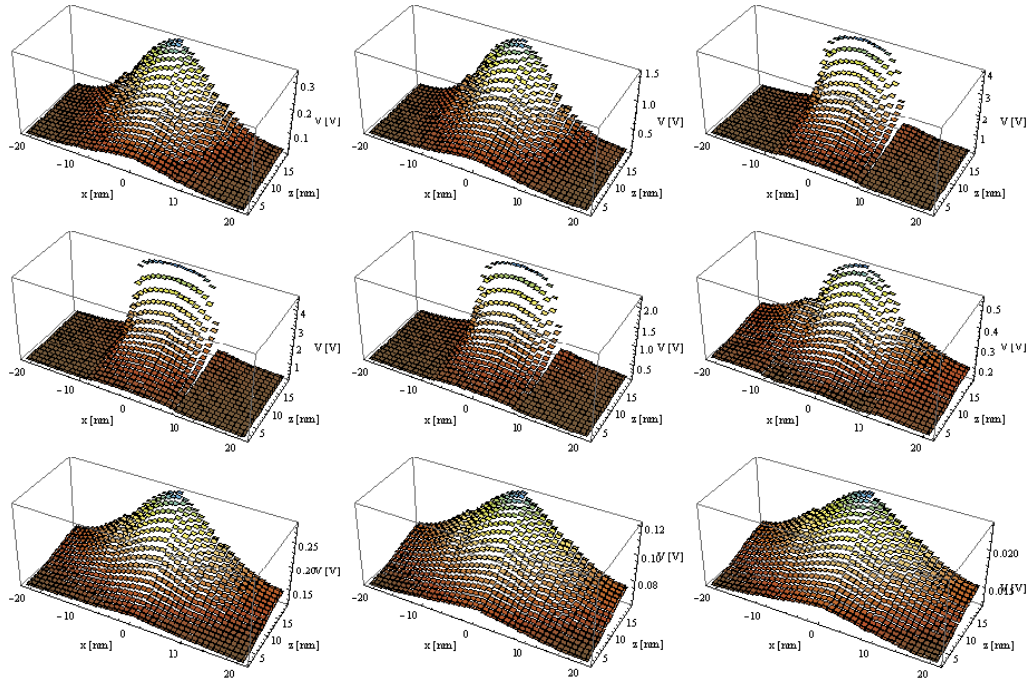
Figure 7.28: Cross sections at $y = 2$nm, $y = 5$nm, $y = 10$nm, $y = 14$nm, $y = 19$nm, $y = 21$nm, $y = 25$nm, $y = 30$nm, and $y = 34$nm showing the electric potential V.
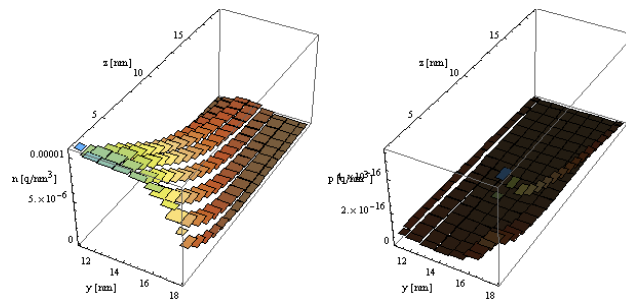

Figure 7.29: Cross sections at $x = 5$nm showing the electron density n and the hole density p.
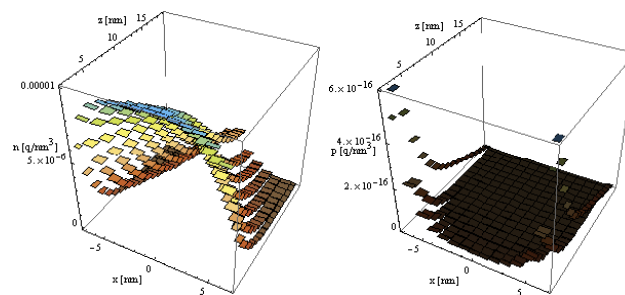
Figure 7.30: Cross sections at $y = 14$nm showing the electron density n and the hole density p.
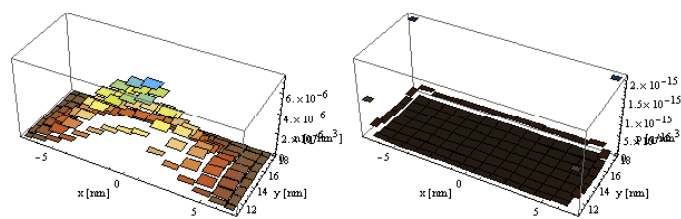
Figure 7.31: Cross sections at $z = 10$nm showing the electron density n and the hole density p.

Results for $V_b = 0\text{V}$, $V_e = 0\text{V}$, $V_s = -5\text{V}$, $V_d = 5\text{V}$

Figure 7.32 and Figure 7.34 show the decrease of the electric potential V in the direction to the source and an increase of the electric potential V in the direction to the drain.
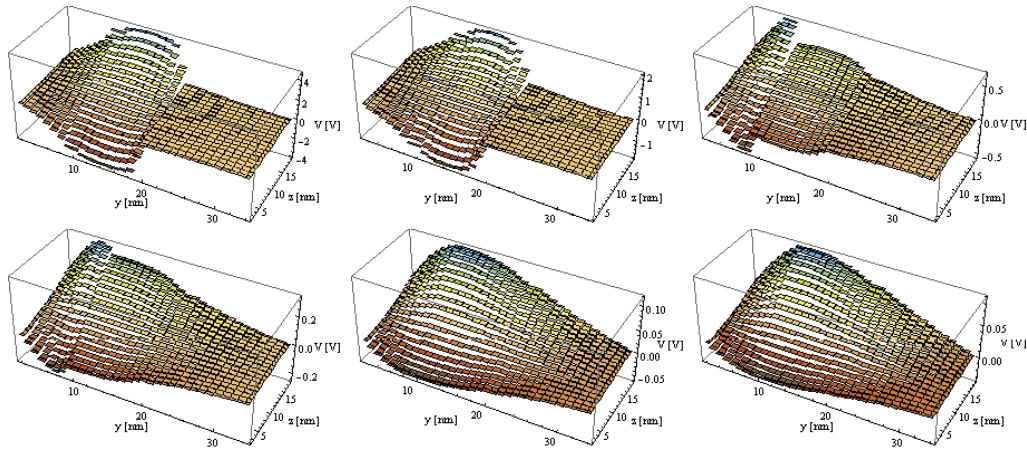

Figure 7.32: Cross sections at $x = 0$nm, $x = 10$nm, $x = 12$nm, $x = 14$nm, $x = 19$ nm, and $x = 23$nm showing the electric potential V.

The same effect can be observed in Figure 7.33 where we have a low average electric potential V on the first picture and a higher average electric potential V at the third picture.

In Figure 7.35, 7.36, and 7.37 we see that we have indeed a current flow from source to drain which results that the hole density p equals zero and the electron density n is positive.
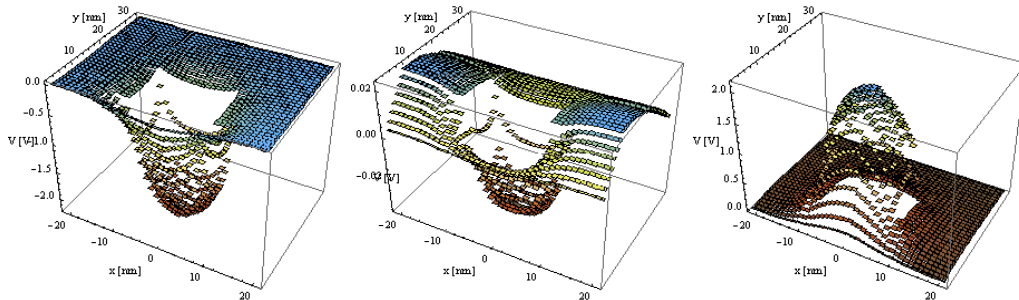

Figure 7.33: Cross sections at $z = 5$nm, $z = 10$nm, and $z = 15$nm showing the electric potential V.
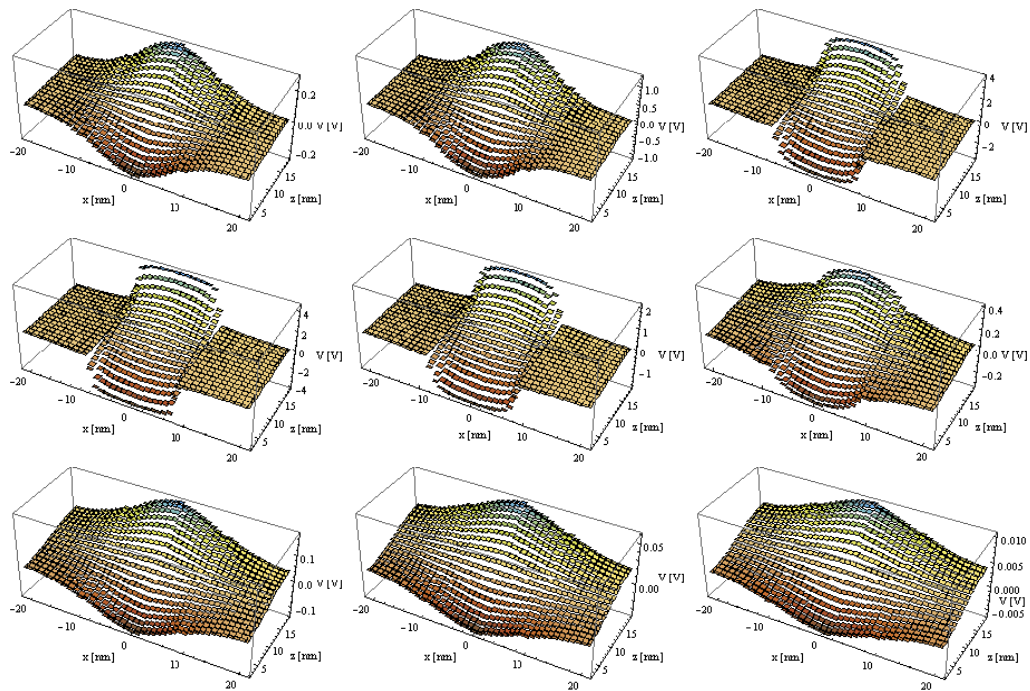
Figure 7.34: Cross sections at $y = 2$nm, $y = 5$nm, $y = 10$nm, $y = 14$nm, $y = 19$nm, $y = 21$nm, $y = 25$nm, $y = 30$nm, and $y = 34$nm showing the electric potential V.
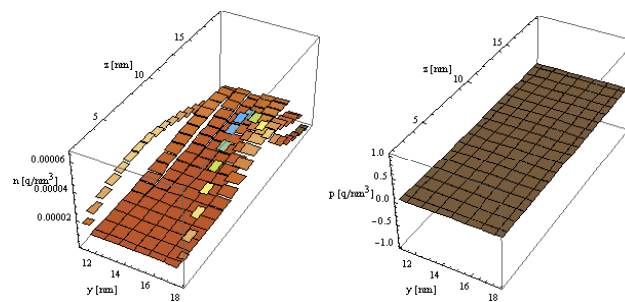

Figure 7.35: Cross sections at $x = 5$nm showing the electron density n and the hole density p.
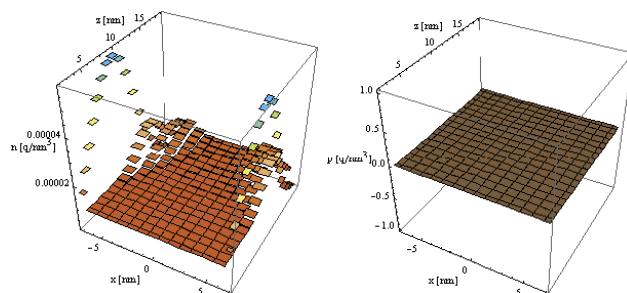
Figure 7.36: Cross sections at $y = 14$nm showing the electron density n and the hole density p.
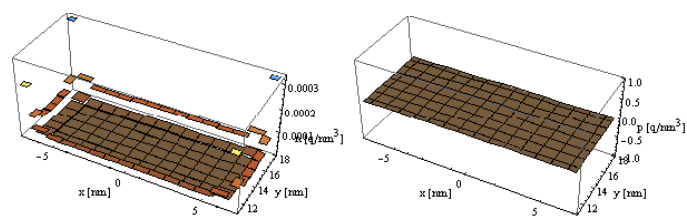
Figure 7.37: Cross sections at $z = 10$nm showing the electron density n and the hole density p.

Results for $V_b = -2\text{V}$, $V_e = 1\text{V}$, $V_s = 0\text{V}$, $V_d = 0\text{V}$

Figure 7.38 shows -2V at the right-hand side and 1V at the left-hand side of the pictures.
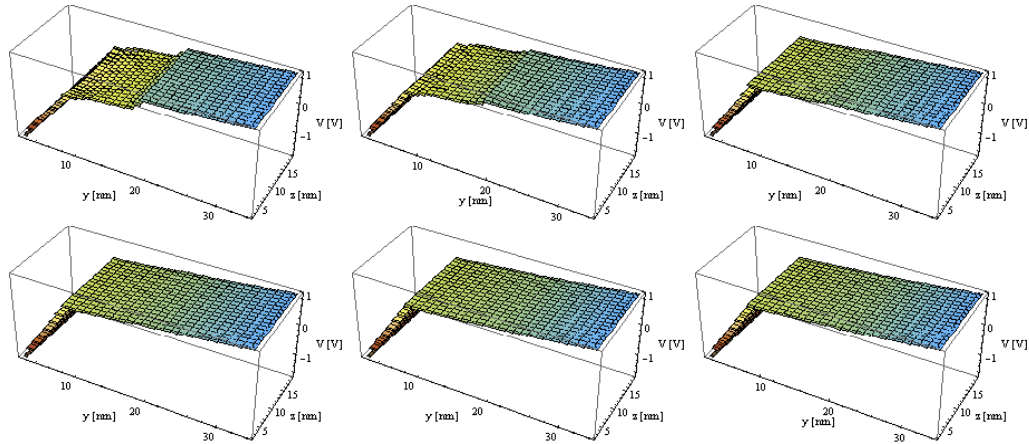

Figure 7.38: Cross sections at $x = 0$nm, $x = 10$nm, $x = 12$nm, $x = 14$nm, $x = 19$ nm, and $x = 23$nm showing the electric potential V.

The same behavior as in Figure 7.38 can be observed in Figure 7.39.

In Figure 7.40 we see that the average electric potential V increases from picture to picture.

The electron density n is again positive and the hole density p has a value nearby zero.
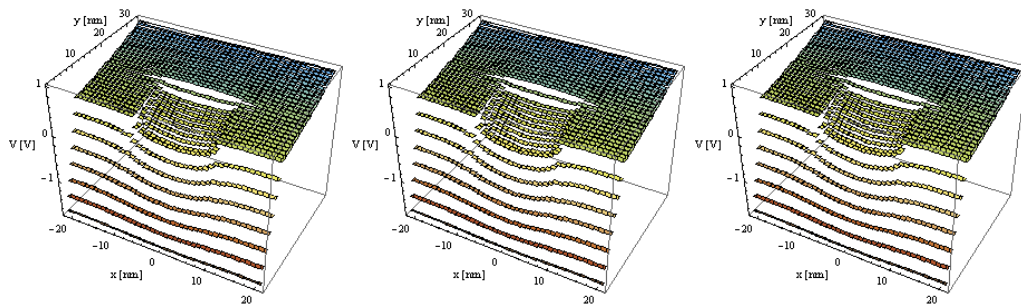
Figure 7.39: Cross sections at $z = 5$nm, $z = 10$nm, and $z = 15$nm showing the electric potential V.
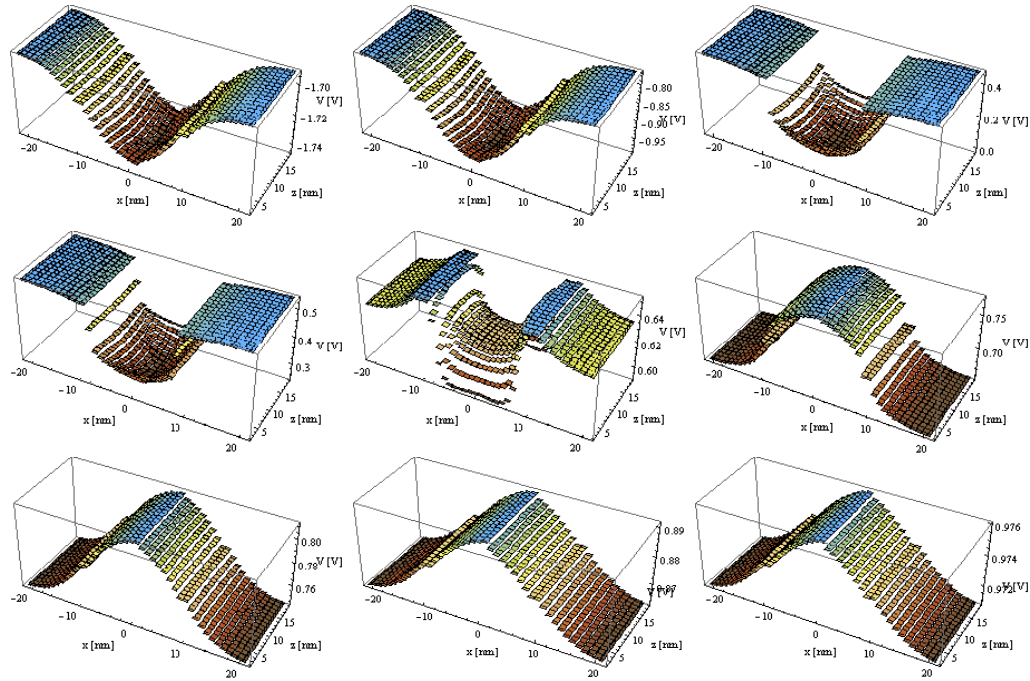
Figure 7.40: Cross sections at $y = 2$nm, $y = 5$nm, $y = 10$nm, $y = 14$nm, $y = 19$nm, $y = 21$nm, $y = 25$nm, $y = 30$nm, and $y = 34$nm showing the electric potential V.
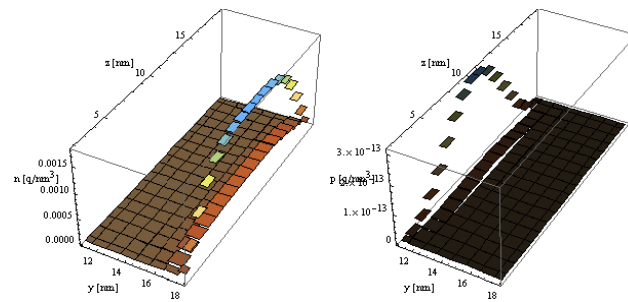

Figure 7.41: Cross sections at $x = 5$nm showing the electron density n and the hole density p.
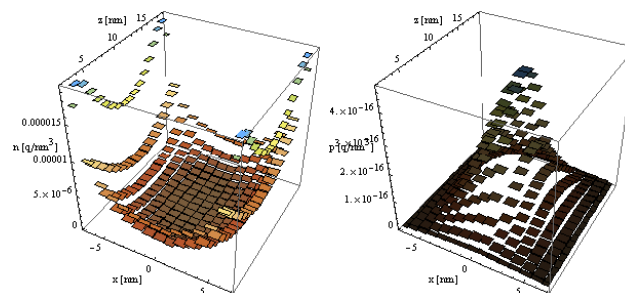
Figure 7.42: Cross sections at $y = 14$nm showing the electron density n and the hole density p.
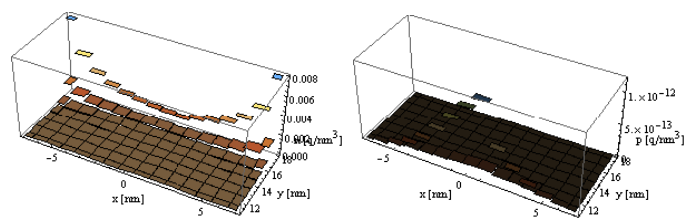
Figure 7.43: Cross sections at $z = 10$nm showing the electron density n and the hole density p.

Results for $V_b = -2.5$V, $V_e = 2.5$V, $V_s = -5$V, $V_d = 5$V

Figure 7.44 shows in the first picture the boundary conditions for source and drain in the silicon domain. Furthermore we can see back-gate and electrode boundary conditions at the left and at the right side of the pictures.
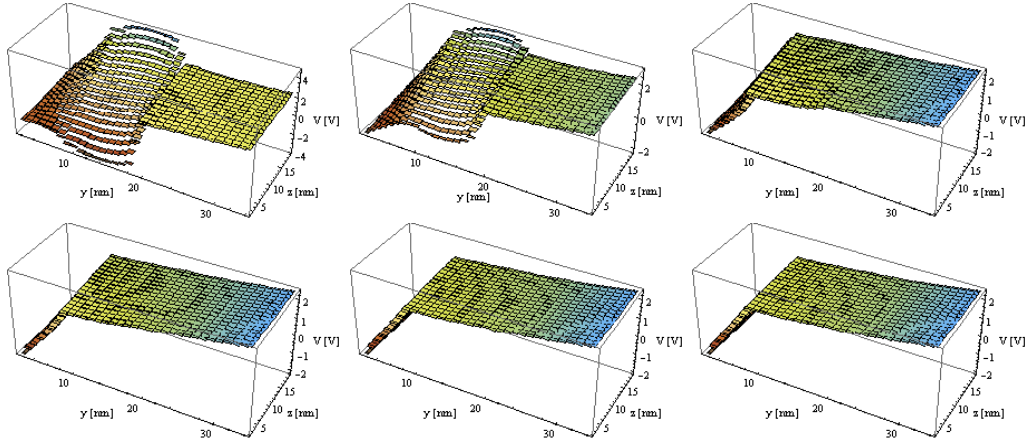
Figure 7.44: Cross sections at $x = 0$nm, $x = 10$nm, $x = 12$nm, $x = 14$nm, $x = 19$ nm, and $x = 23$nm showing the electric potential V.

The same behavior like in Figure 7.44 can be observed in Figure 7.45 and in Figure 7.46.

The hole density p and the electron density n are similar to the figures 7.35, 7.36, and 7.37.
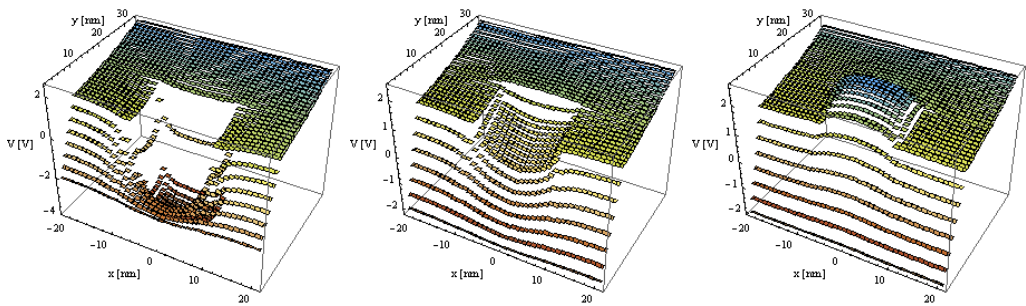
Figure 7.45: Cross sections at $z = 5$nm, $z = 10$nm, and $z = 15$nm showing the electric potential V.
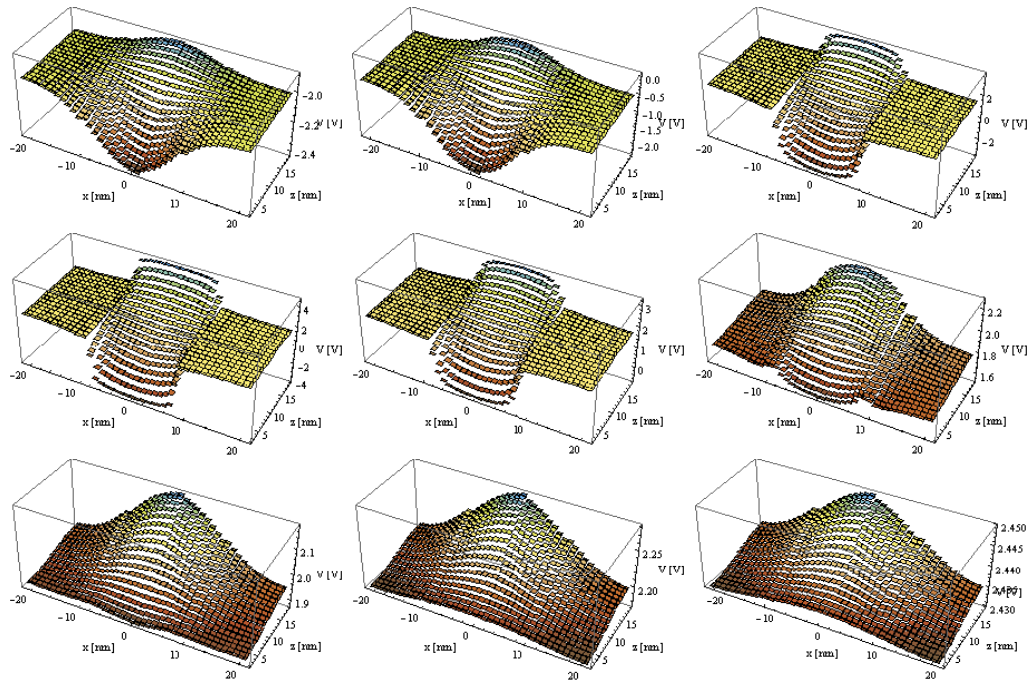
Figure 7.46: Cross sections at $y = 2$nm, $y = 5$nm, $y = 10$nm, $y = 14$nm, $y = 19$nm, $y = 21$nm, $y = 25$nm, $y = 30$nm, and $y = 34$nm showing the electric potential V.
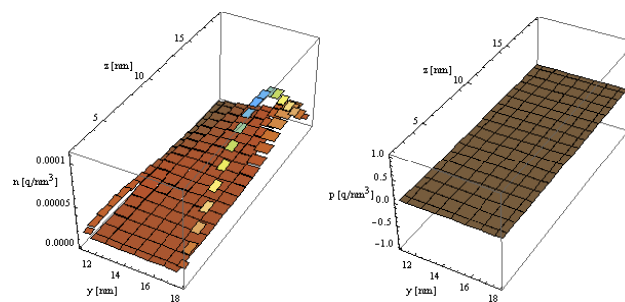
Figure 7.47: Cross sections at $x = 5$nm showing the electron density n and the hole density p.
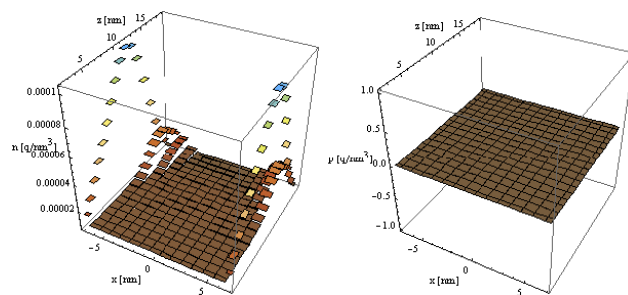
Figure 7.48: Cross sections at $y = 14$nm showing the electron density n and the hole density p.
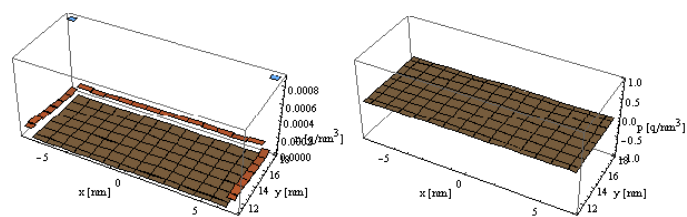

Figure 7.49: Cross sections at $z = 10$nm showing the electron density n and the hole density p.

7.2 Current flow

Here we show the current flow in three cross sections for each coordinate direction
with the boundary conditions $V_b = -2.5$V, $V_e = 2.5$V, $V_s = -5$V, and $V_d = 5$V.
The majority carriers are the electrons and therfore the current flow of the holes
vanishes. Hence we show only the electron flow.
The current flow is shown in the three coordinate directions. As an example we
can take the current flow in x-direction

$$J^n_{i+\frac{1}{2},j,k} = -q\mu_n \frac{V_{i+1,j,k} - V_{i,j,k}}{dx} \cdot \frac{e^{c_n V_{i+1,j,k}} n_{i+1,j,k} - e^{c_n V_{i,j,k}} n_{i,j,k}}{e^{c_n V_{i+1,j,k}} - e^{c_n V_{i,j,k}}}$$

and the current flow in y and z-direction are computed analogously.
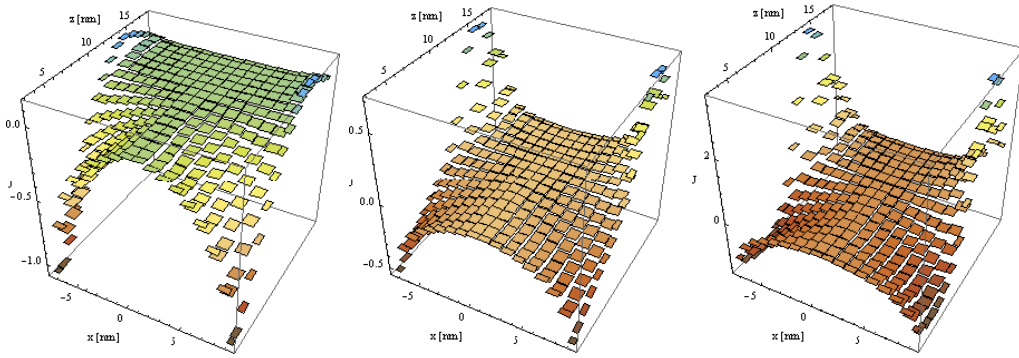
Figure 7.50: Electron flow in x-direction at $y = 10$nm, $y = 13$nm, and $y = 17$nm.
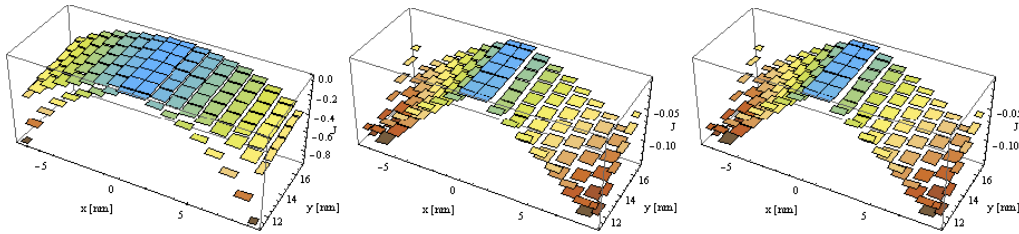
Figure 7.51: Electron flow in x-direction at $z = 5$nm, $z = 10$nm, and $z = 15$nm.
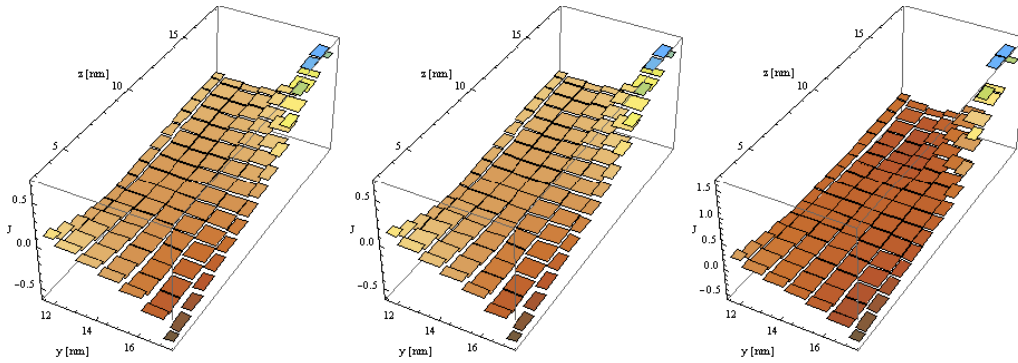
Figure 7.52: Electron flow in y-direction at $x = 0$nm, $x = 4$nm, and $x = 8$nm.
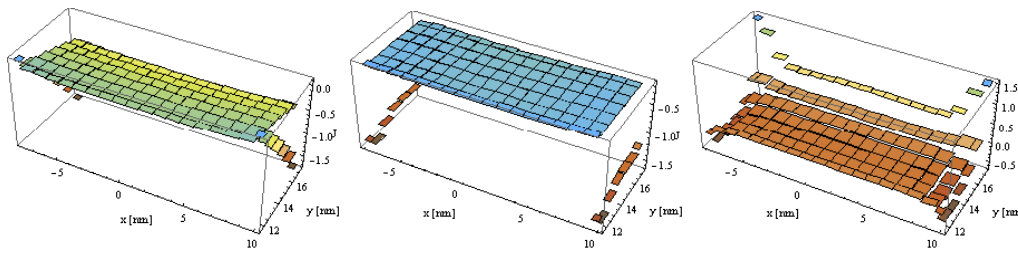
Figure 7.53: Electron flow in y-direction at $z = 5$nm, $z = 10$nm, and $z = 15$nm.
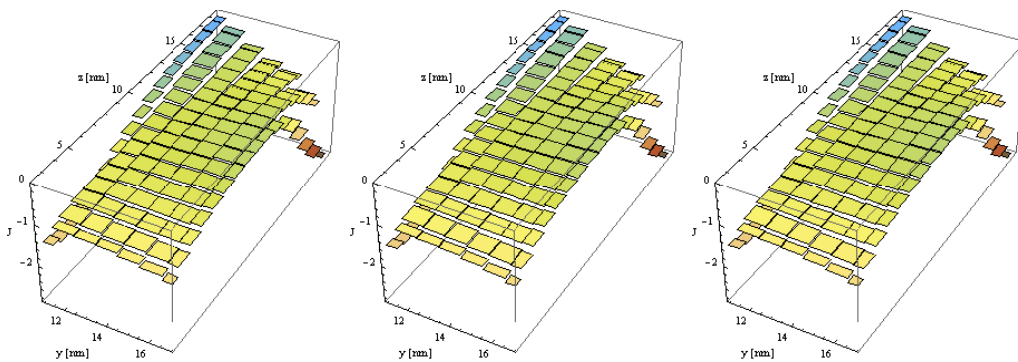

Figure 7.54: Electron flow in z-direction at $x = 0$nm, $x = 4$nm, and $x = 8$nm.
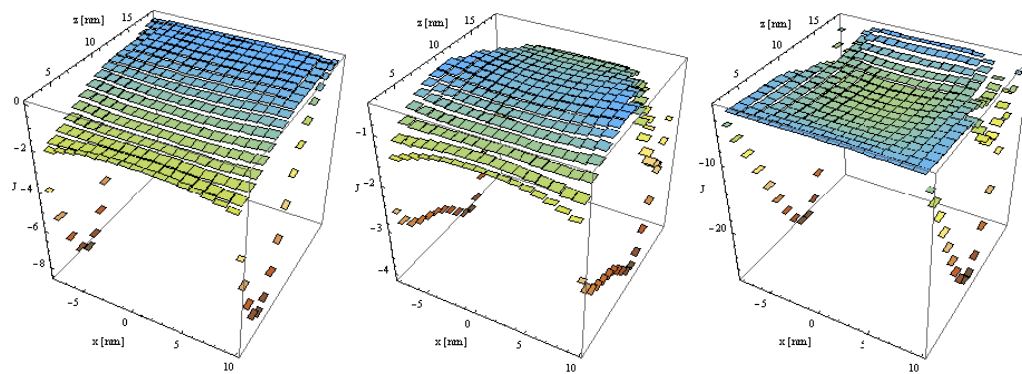
Figure 7.55: Electron flow in z-direction at $y = 10$nm, $y = 13$nm, and $y = 17$nm.

7.3 Influence of Na^+Cl^- concentration

This paragraph shows the electric potential V and the current in three cross sections for varying Na^+Cl^- concentration with $V_b = -2.5V$, $V_e = 2.5V$, $V_s = -5V$, and $V_d = 5V$.
We see in the cross sections $x = 0nm$ and $z = 10nm$ that with decreasing Na^+Cl^- concentration the influence of the boundary condition V_e at the electrode on the electric potential V and the electric potential V at the cross section $y = 30nm$ increases. This results in a decreasing current I_{SD} which is shown in Table 7.4.

α (in mole $\cdot$ nm^{-3})	I $[\mu A]$
$6.02214 \cdot 10^{-2}$	-31.7023
$6.02214 \cdot 10^{-3}$	-31.5678
$6.02214 \cdot 10^{-4}$	-35.033
$6.02214 \cdot 10^{-5}$	-40.3515
$6.02214 \cdot 10^{-6}$	-41.6232

Table 7.4: Current for varying Na^+Cl^- concentration.
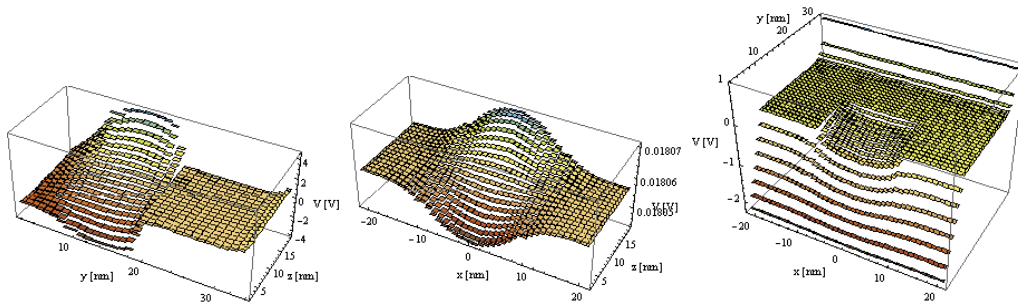
Figure 7.56: Cross sections at $x = 0nm$, $y = 30nm$, and $z = 10nm$ showing the electric potential V with Na^+Cl^- concentration $\alpha = 6.02214 \cdot 10^{-2}mol \cdot nm^{-3}$.
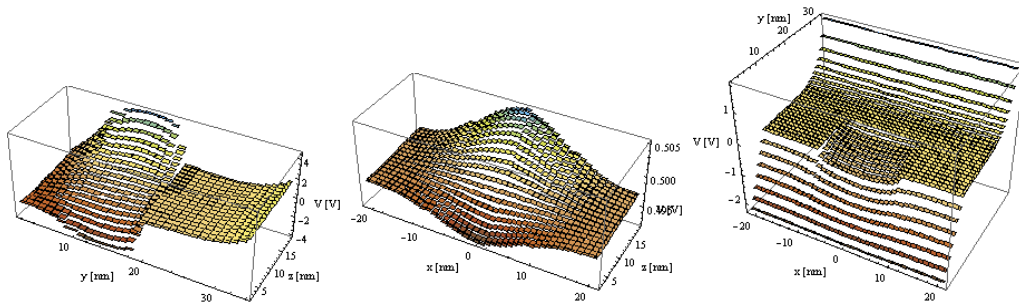
Figure 7.57: Cross sections at $x = 0$nm, $y = 30$nm, and $z = 10$nm showing the electric potential V with Na$^+$Cl$^-$ concentration $\alpha = 6.02214 \cdot 10^{-3}$mol $\cdot$ nm^{-3}.
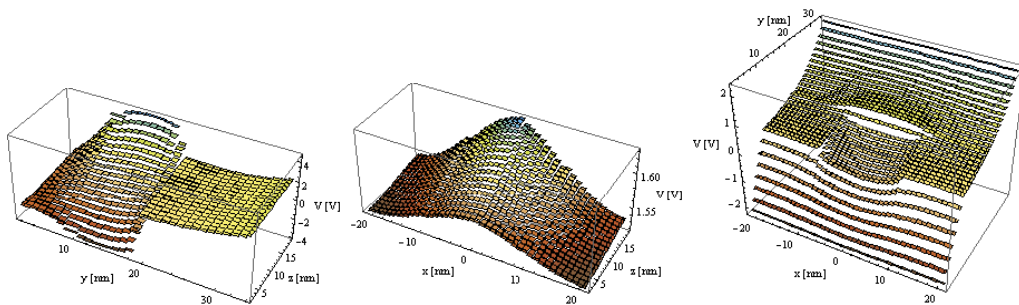
Figure 7.58: Cross sections at $x = 0$nm, $y = 30$nm, and $z = 10$nm showing the electric potential V with Na$^+$Cl$^-$ concentration $\alpha = 6.02214 \cdot 10^{-4}$mol $\cdot$ nm^{-3}.
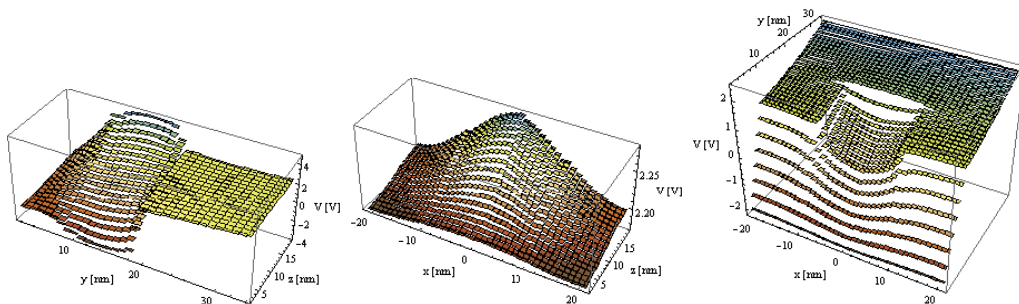
Figure 7.59: Cross sections at $x = 0$nm, $y = 30$nm, and $z = 10$nm showing the electric potential V with Na$^+$Cl$^-$ concentration $\alpha = 6.02214 \cdot 10^{-5}$mol $\cdot$ nm^{-3}.
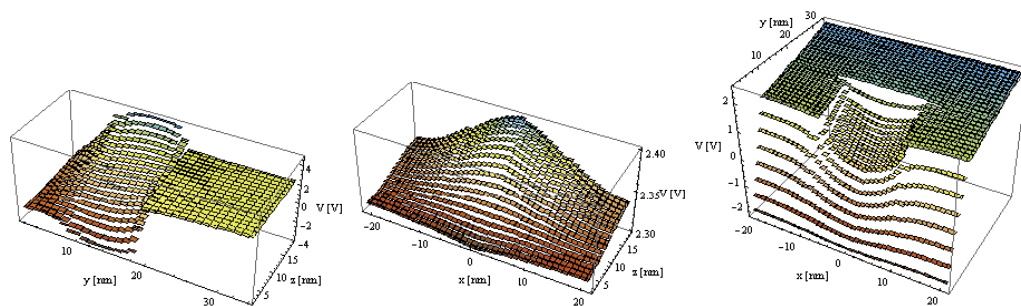
Figure 7.60: Cross sections at $x = 0$nm, $y = 30$nm, and $z = 10$nm showing the electric potential V with Na^+Cl^- concentration $\alpha = 6.02214 \cdot 10^{-6}$mol $\cdot$ nm^{-3}.

7.4 Interface

Here we discuss the source-drain current for varying macroscopic surface charge density C_s and varying macroscopic dipole moment density D. Therefore we use the boundary conditions $V_b = -2.5\text{V}$, $V_e = 2.5\text{V}$, $V_s = -5\text{V}$, and $V_d = 5\text{V}$. In Figure 7.61 and Figure 7.62 the macroscopic dipole moment density varies from $-1\text{q} \cdot \text{nm}^{-1}$ to $1\text{q} \cdot \text{nm}^{-1}$ in $0.25\text{q} \cdot \text{nm}^{-1}$ steps. The lines in Figure 7.61 from top to bottom and in Figure 7.62 from bottom to top are the currents for different values of the macroscopic surface charge density from $-0.1\text{q} \cdot \text{nm}^{-2}$ to $0.15\text{q} \cdot \text{nm}^{-2}$ in $0.025\text{q} \cdot \text{nm}^{-2}$ steps. The difference between these two figures is that in Figure 7.61 the semiconductor is p-doped with $C = -10^{16}\text{q} \cdot \text{nm}^{-3}$ and in Figure 7.62 the semiconductor is n-doped with $C = 10^{16}\text{q} \cdot \text{nm}^{-3}$.
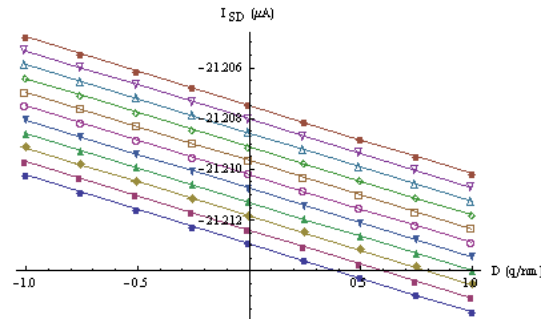

Figure 7.61: Source-drain current for a p-doped nanowire biosensor with varying macroscopic surface charge density and varying dipole moment density.
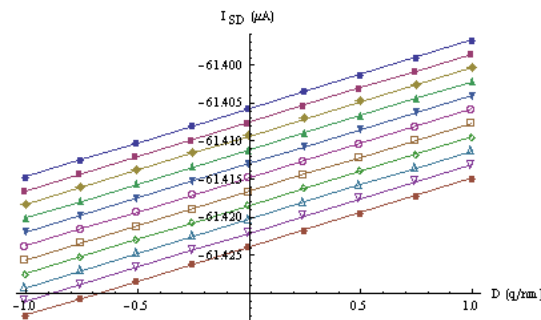

Figure 7.62: Source-drain current for a n-doped nanowire biosensor with varying macroscopic surface charge density and varying dipole moment density.

7.5 Current

In order to relate the simulations to measurements, we show the IV characteristics of the sensor structure. Figure 7.63 shows the source-drain current for varying back-gate voltage and varying source voltage. Furthermore we set $V_d := 0$V and $V_e := 0$V. The blue line on the top of the left side of the figure is for $V_b = -3$V. The lines beneath are for $V_b = -2$V, $V_b = -1$V, $V_b = 0$V, $V_b = 1$V, $V_b = 1.2$V, $V_b = 1.5$V, $V_b = 1.8$V, and $V_b = 2$V.
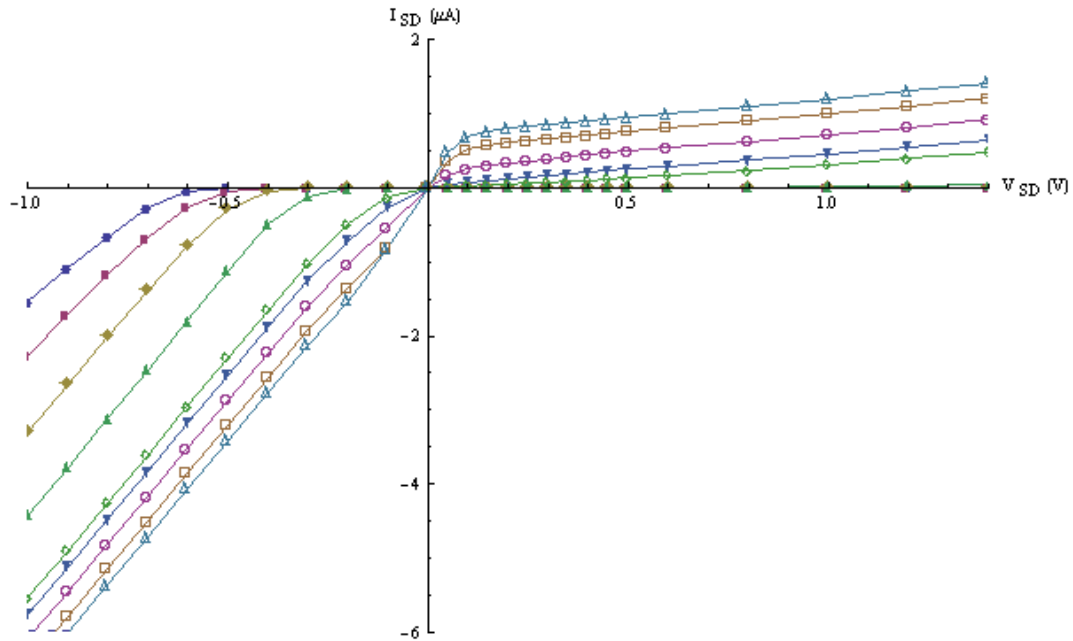
Figure 7.63: Current from $V_s = -1$V to $V_s = 1.4$V for varying back-gate voltage from $V_b = -3$V to $V_b = 1$V in 1 V steps and $V_b = 1.2$V, $V_b = 1.5$V, $V_b = 1.8$V, and $V_b = 2$V.

Table 7.5 shows the current for different lengths. Here we used $V_s = -0.75$V, $V_d = 0$V, and $V_e = 0$V. We see that the difference between the currents of biosensors with $L_z = 80$nm and $L_z = 100$nm is for $V_b = -3$nm bigger than for $V_b = 0$nm.

V_b [V]	$L_z = 20$nm	$L_z = 40$nm	$L_z = 60$nm	$L_z = 80$nm	$L_z = 100$nm
-3	-0.464569	-0.0456427	-0.0128917	-0.00675331	-0.00450685
-2	-0.921903	-0.530093	-0.410956	-0.33454	-0.28108
-1	-1.69527	-1.35971	-1.32128	-1.30011	-1.2802
0	-2.79327	-2.5672	-2.54012	-2.52439	-2.51022

Table 7.5: I_{SD} [μA] for different boundary conditions at the back-gate and varying L_z.

Finally we show in Figure 7.64 varying back-gate voltage and varying source voltage for a p-doped nanowire with $C = -10^{16}$q $\cdot$ nm^{-3}. The voltages at the drain and the electrode are again $V_e = 0$V and $V_d = 0$V. Furthermore the back-gate voltage varies in the lines on the right side from top to bottom from $V_b = -2$V to $V_b = 3$V in 1 V steps.
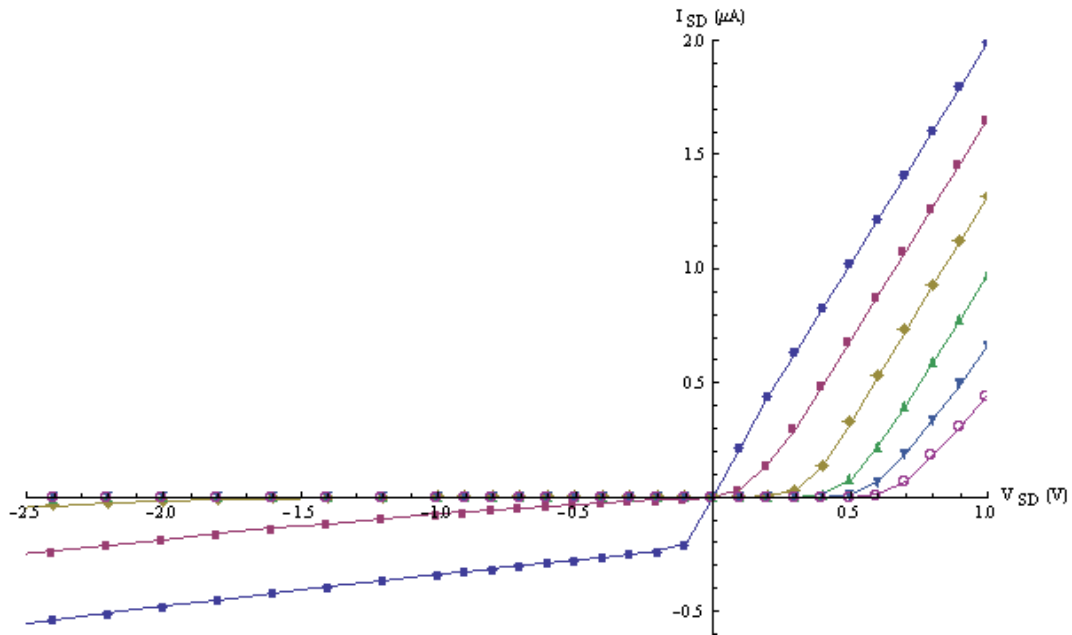
Figure 7.64: Current from $V_s = -2.5$V to $V_s = 1$V for varying back-gate voltage from $V_b = -2$V to $V_b = 3$V in 1 V steps.

Figure 7.63 and Figure 7.64 are in a qualitative agreement with the measurements in Figure 2a and Figure 2b of [4], one of the most important experiments in this field to date.

7.6 Conclusion

The agreement of Figure 7.63 and 7.64 with measured values shows that the essential physics of field-effect biosensors are included in our PDE-based model. We point out that it is a full 3D model that includes the back-gate contact. This work is therefore an important building block of the self-consistent three-dimensional modeling and simulation of nanowire field-effect biosensors.

The multi-scale problem inherent in these biosensors was solved by implementing interface conditions derived from the homogenization of the biofunctionalized boundary layer. The interface conditions were implemented efficiently by a special numbering scheme of the equations of the discretization. An efficient implementations is especially important for 3D simulations.

We also investigated how different parameter values for the boundary, the interface, and the Na^+Cl^- concentration influence the source-drain current I_{SD}. The I_{SD} current was calculated because this value is usually measured.

The computation of the macroscopic surface charge density C_s and the macroscopic dipole moment density D is not discussed in this work. These values have been calculated from Poisson-Boltzmann and Monte-Carlo simulations.

In future work we will identify certain physical parameters of BioFETs to arrive at a calibrated model and to make predictive simulations of 3D structures possible.

Bibliography

[1] G. Dahlquist and Å. Björck, *Numerical methods in scientific computing*, vol. 1, SIAM, 2008.

[2] C. Heitzinger, N.J. Mauser, and C. Ringhofer, *Multi-scale modeling of planar and nanowire field-effect biosensors*.

[3] P. Knabner and L. Angermann, *Numerik partieller Differentialgleichungen: Eine anwendungsorientierte Einführung*, Springer, 2000.

[4] Y. Li, F. Qian, J. Xiang, and C.M. Lieber, *Nanowire electronic and optoelectronic devices*, Materials today **9** (2006), no. 10, 18–27.

[5] P.A. Markowich, C.A. Ringhofer, and C. Schmeiser, *Semiconductor equations*, Springer-Verlag New York, Inc. New York, NY, USA, 1990.

[6] F. Patolsky, G. Zheng, and C.M. Lieber, *Nanowire sensors for medicine and the life sciences*, Nanomedicine **1** (2006), no. 1, 51–65.

[7] R. Schaback and H. Wendland, *Numerische Mathematik*, vol. 5, Springer, 2005.

[8] D.L. Scharfetter and H.K. Gummel, *Large-signal analysis of a silicon read diode oscillator*, IEEE Transactions on Electron Devices **16** (1969), no. 1, 64–77.

[9] M.J. Schöning and A. Poghossian, *Recent advances in biologically sensitive field-effect transistors (BioFETs)*, The Analyst **127** (2002), no. 9, 1137–1151.

[10] M.J. Schöning and A. Poghossian, *Bio-feds (field-effect devices): State-of-the-art and new directions*, Electroanalysis **18** (2006), 1893–1900.

[11] E. Stern, J.F. Klemic, D.A. Routenberg, P.N. Wyrembak, D.B. Turner-Evans, A.D. Hamilton, D.A. Lavan, T.M. Fahmy, and M.A. Reed, *Label-free immunodetection with cmos-compatible semiconducting nanowires*, Nature(London) **445** (2007), no. 7127, 519–522.

[12] E. Stern, E.R. Steenblock, M.A. Reed, and T.M. Fahmy, *Label-free electronic detection of the antigen-specific t-cell immune response*, Nano Letters **8** (2008), no. 10, 3310–3314.

[13] D.R. Thévenot, K. Toth, R.A. Durst, and G.S. Wilson, *Electrochemical biosensors: recommended definitions and classification*, Biosensors and Bioelectronics **16** (2001), no. 1-2, 121–131.

[14] H.A. van der Vorst, *Iterative krylov methods for large linear systems*, Cambridge University Press, 2003.

[15] G. Zheng, F. Patolsky, Y. Cui, W.U. Wang, and C.M. Lieber, *Multiplexed electrical detection of cancer markers with nanowire sensor arrays*, Nature biotechnology **23** (2005), no. 10, 1294–1301.

CURRICULUM VITAE

Stefan Andreas Baumgartner

Geboren am 14. April 1985 in Scheibbs

Staatsbürgerschaft: Österreich

AUSBILDUNG:

November 2007	Abschluss des ersten Studienabschnitts im Diplomstudium Mathematik
Oktober 2005	Beginn der Diplomstudien Mathematik und Musikwissenschaft
September 2004 - April 2005	Präsenzdienst in der Birago Kaserne Melk
Juni 2004	Reifeprüfung an der HTBLuVA St.Pölten Abteilung EDVO